Quantum Efficiency of Josephson Traveling Wave Parametric Amplifiers with Many-Mode Processes

by

Kaidong Peng

B.S., University of Illinois Urbana-Champaign (2018)

Submitted to the Department of Electrical Engineering and Computer Science
in partial fulfillment of the requirements for the degree of

Master of Science in Electrical Engineering

at the

MASSACHUSETTS INSTITUTE OF TECHNOLOGY

May 2020

Author .....
Department of Electrical Engineering and Computer Science
May 15, 2020

Certified by .....
Kevin P. O'Brien
Assistant Professor of Electrical Engineering and Computer Science
Thesis Supervisor

Accepted by .....
Leslie A. Kolodziejski
Professor of Electrical Engineering and Computer Science
Chair, Department Committee on Graduate Students

Quantum Efficiency of Josephson Traveling Wave Parametric Amplifiers with Many-Mode Processes

by

Kaidong Peng

Submitted to the Department of Electrical Engineering and Computer Science
on May 15, 2020, in partial fulfillment of the
requirements for the degree of
Master of Science in Electrical Engineering

Abstract

Josephson traveling wave parametric amplifiers (JTWPAs) are widely used in superconducting qubit and microwave quantum optics experiments. Compared with cavity-based Josephson parametric amplifiers (JPAs), JTWPAs have ∼10dB higher dynamic range and an order of magnitude higher bandwidth, exhibiting >20dB gain over several gigahertz of instantaneous bandwidth. The broad bandwidth and high dynamic range of JTWPAs allow for simultaneous readout of more than 20 frequency-multiplexed qubits. With these amplifiers, qubit readout fidelities above 99% have been achieved; however, current JTWPA have a full readout chain quantum efficiency of ∼50% which is well below that of an ideal parametric amplifier. This thesis studies the effect of higher order modes on the quantum efficiency, identifies mitigation strategies, and proposes new designs of JTWPAs with improved quantum efficiency that can potentially increase qubit readout speed and fidelity.

Thesis Supervisor: Kevin P. O'Brien
Title: Assistant Professor of Electrical Engineering and Computer Science

Acknowledgments

I would like to express my sincerest gratitude to my advisor Professor Kevin O'Brien, and my parents for all their support. I would also like to acknowledge the tremendous support I received from my girlfriend Rui Huang, without whom this thesis wouldn't even be possible.

Contents

List of Figures

List of Tables

Chapter 1

Introduction

Quantum computing, a new computing paradigm, utilizes the phenomena of superposition and entanglement to perform computation. The recent invention of powerful quantum algorithms [59, 23, 17] has spurred significant development and investment in quantum computing, which has the potential to expand what is considered computable. Moreover, quantum computers are well suited for simulating other quantum systems which can advance fields such as pharmaceutical science, materials science, and particle physics [70, 40].

Quantum computers can be implemented with many different physical systems [32, 44, 52, 8], among which superconducting quantum circuits are considered one of the leading platforms [46]. The quantum electrodynamics of superconducting quantum circuits is termed circuit quantum electrodynamics (cQED) [6]. In superconducting quantum computing, qubits are typically made from Josephson junctions, which are nonlinear electric elements formed by a thin dielectric layer between by two superconductor leads [30]. The strong nonlinearity of Josephson junctions makes it possible to construct artificial atoms whose transition between the lowest two energy levels can be distinguished and controlled separately from the others. The cQED platform is promising for a number of reasons including fast control and readout. The readily achievable strong coupling between photons and superconducting qubits currently allows hundreds to thousands of readout and gate operations before the qubits decohere. In addition, modern nanofabrication and integrated circuits tech-

niques enable the scalable fabrication of large-scale quantum circuits with hundreds of superconducting qubits on a single chip.

Regardless of the platform, the ability to perform qubit state readout with high fidelity at a fast rate is essential for any quantum information processing tasks. In circuit QED, a qubit state is typically determined from the state-dependent dispersive phase shift of a readout resonator coupled to the qubit [58, 6, 33]. A weak microwave probe tone is reflected off of the readout resonator and the qubit state information is encoded in its phase. The weak microwave tone needs to be amplified in a series of stages before detection and digitization by room temperature electronics. The signal-to-noise ratio (SNR) of the detected signal at the final stage is mostly determined by the first amplifier in the amplifier chain [14]. The SNR directly affects how well and how quickly different qubit states can be differentiated from each other. This necessitates the use of an ultra-low noise amplifier at the front end of the chain. To date, near quantum-limited amplifiers in the microwave frequency range are all based on the principle of nonlinear parametric amplification [69, 13, 65, 20, 47, 38, 66]. In a parametric amplifier, the weak signal of interest interacts with one or more strong and coherent pump tones at different frequencies through a three- or four-wave mixing process. Because the amplification process is parametric, the associated noise can be quantum-limited if the system is lossless and no other interactions are present [25, 14].

Josephson parametric amplifiers (JPAs) with near quantum-limited noise performance have been used for superconducting qubit readout since as early as 2011 [1]. JPAs are essentially nonlinear parametric oscillators in which the intermodulation between pump and signals is enhanced by a cavity [65, 20]. JPAs can typically achieve $>$20dB gain over a 3dB bandwidth of several MHz, subject to the gain-bandwidth product imposed by the existence of the cavity. Although operating at near quantum-limited noise and therefore suitable for single qubit readout, JPAs unfortunately have relatively small dynamic range and thus a slow response time due to the resonant interactions in the cavity. Although JPAs with widely tunable frequency range [11] or bandwidth as large as 640 MHz [56] have been realized to overcome the limitation of the narrow instantaneous bandwidth, they are still not suitable for larger-scale

quantum circuits because in a typical experiment large subsets of the qubits must be measured simultaneously which requires both a bandwidth and a high dynamic range. A large quantum computer using JPAs for readout would require order of one amplifier and readout line per qubit.

Josephson traveling wave parametric amplifiers (JTWPAs)[47, 38, 66] have been widely used in superconducting quantum experiments [24, 64, 43, 27, 15] since their first demonstration in 2015. In contrast to JPAs which use a cavity to enhance the interaction time, JTWPAs adopt a traveling wave architecture such that the interaction between the weak signal and strong pump is enhanced by an extended interaction length, typically on the order of a thousand junctions or tens of wavelengths [38]. Avoiding resonant interactions, albeit with an increased device footprint, brings several advantages to the JTWPAs. While still operating at near quantum-limited noise performance, JTWPAs have >20 dB gain over an instantaneous bandwidth of several gigahertz, which is orders of magnitude larger than that of a typical JPA. Moreover, JTWPAs have ∼10 dB higher dynamic range than a typical JPA. The broad instantaneous bandwidth and high dynamic range of JTWPAs allow for simultaneously readout of more than 20 frequency-multiplexed qubits, making it more scalable for future larger-scale quantum circuits. In addition, JTWPAs have a much shorter response time and are better suited for fast quantum feedback experiments. Experiments using a JTWPA as the front-end amplifier have achieved >97% average readout fidelity of five frequency multiplexed qubits in 250 ns [27], limited predominantly by qubit lifetime and measurement induced mixing.

The intrinsic quantum efficiency of a typical JTWPA is 75% [38], taking into account the distributed loss contribution of 90%. This means there is an unaccounted inefficiency of about 83% in amplifier operation, which is much lower than that of an ideal parametric amplifier. To improve the speed and reliability of quantum circuits and algorithms, one has to optimize the efficiency of every single component in the measurement chain especially the JTWPA as it is the front end amplifier and thus has the largest influence on the measurement SNR. Due to the fabrication complexity and high uniformity requirement, most JTWPAs to date are fabricated in a

specialized, tri-layer niobium process with non-negligible dielectric loss [61]. Alternatively, JTWPAs can be fabricated in an atomic-layer-deposition alumina process [50] which nevertheless has a comparable dielectric loss. The inefficiency resulted from distributed loss, which is not a fundamental limitation, is anticipated to be largely mitigated by shifting to a higher quality fabrication process (i.e. a typical qubit process) in the future. However, the origin of the additional efficiency reduction is still not well understood and the lack of understanding the development of mitigation strategies.

1.1 Thesis Overview

This thesis is centered around the quantum efficiency of Josephson traveling wave parametric amplifiers (JTWPAs). The first major goal of this thesis is to understand the origin of the unknown reduction in the intrinsic quantum efficiency of a typical JTWPA and develop a model. The second major goal is to develop schemes to mitigate the identified issues and propose a new JTWPA design with improved quantum efficiency.

In chapter 2, we will review the cQED formulation with a focus on the topics most relevant to the later discussion of JTWPAs. I will describe the constitutive relations of the Josephson junctions, describe a typical measurement set up of a typical quantum experiment, and give a high-level explanation of where the JTWPAs fit into the picture.

In chapter 3, we will review both the classical and quantum theory of a standard JTWPA and derive the nonlinear wave equations and the circuit Hamiltonian. We then present simplified two-mode equations of motion and discuss the major approximations made in this derivation. Recognizing these approximations will help us understand the amplifier non-idealities seen in experiments that are not captured by the simplified two-mode model.

In chapter 4, we will first discuss and evaluate the validity of each of the aforementioned approximations for a typical JTWPA [38]. We will then present a generalized,

multi-mode model that incorporates several of these non-idealities including higher harmonics of the pump, higher order sidebands, and the invalidity of the slowly varying envelope approximation (SVEA). We then apply this model to calculate the system dynamics and compare it with the two-mode result.

In chapter 5, we will use the generalized model developed in chapter 4 to calculate the noise figure and the adjusted quantum efficiency of a typical JTWPA and discuss its agreement with the experimental extracted value in [38]. Finally, we discuss potential fixes to the identified issues and propose a new JTWPA design with potentially much improved quantum efficiency.

1.2 Summary of Key Results

In his thesis, we developed a generalized multi-mode model to capture the dynamics of JTWPAs in the presence of many-mode processes and non-ideal pump conditions. We then applied this model to analyze the quantum efficiency of a typical JTWPA and uncover the cause of the previously unaccounted for quantum efficiency reduction: higher order sidebands of the signal. We then showed that we can suppress the generation of higher pump harmonics by introducing a photonic bandgap near the frequency of the third harmonics of the pump. We further suppress the coupling to higher order sidebands by decreasing the cut-off frequency of the transmission line. Finally we integrated the discussed dispersion engineering techniques and proposed a realistic new JTWPA design. we showed that the new JTWPA design has comparable gain bandwidth but is projected to have improved intrinsic quantum efficiency.

Chapter 2

Circuit Quantum Electrodynamics

2.1 Josephson Junctions

In this section, we introduce the physics of Josephson Junctions by first providing an overview of the motivations behind using superconductors for quantum applications. We then describe the constitutive relations of Josephson junctions and show that they are equivalent to a purely-reactive nonlinear inductor in a circuit model. We finally present the Hamiltonian description of a Josephson junction. The treatment on the constitutive relations of Josephson junctions in this section follows closely the procedure used in [18] and [35].

2.1.1 Brief Remarks on Superconductivity

Superconductivity was first experimentally discovered in mercury in 1911 [31] by the Dutch physicist Heike Kamerlingh Onnes, but it was nearly 50 years later in 1957 that the first detailed microscopic theory [5] which can explain the phenomena properly was proposed by John Bardeen, Leon N. Cooper, and Robert Schrieffer. Their microscopic theory is named BCS theory, and it has won them the Nobel Prize in physics in 1972. Following the microscopic theory in 1962, Brian Josephson made the theoretical prediction that a form of supercurrent can flow indefinitely long without voltage applied and can flow through a thin insulating layer between two

pieces of superconductors. This phenomenon, named the Josephson effect, was later experimentally observed and checked by Philip Anderson and John Rowell[3]. For this work, Brian Josephson won the Nobel Prize in Physics in 1973.

The Josephson effect, in essence a macroscopic phenomenon, is at the heart of the development in superconducting circuits and qubits. It turns out that the full-scale microscopic theory is not necessary to describe the behaviors of the collective macroscopic degrees of freedom in quantum circuits [37]. The theory of superconductivity is so rich that it is nearly impossible to cover and discuss all the essential information. Instead of going into the very details of the theory, we will present some brief remarks [18, 35] that will give readers a qualitative understanding of why superconductivity is essential to quantum circuits and circuit QED.

Dissipation and the resulting energy loss are detrimental to quantum coherence and should be avoided whenever possible. The main reason why superconductors are used in circuit QED is that they have zero resistance and can propagate electrons as Cooper pairs [16] across the chip in a dissipationless fashion. This means loss of information from dissipation is avoided and information can be preserved for a much longer time. Because superconductivity usually occurs at very low temperature, the kT thermal noise is significantly reduced to a level much less than the transition energy between the two quantum states of interest(i.e. of a qubit). Furthermore, at such low temperatures, the thermal noise energy (at thermal equilibrium) is also much smaller than the energy gap between the superconducting ground state and the dissipative normal conduction state, making quantum circuits greatly resistant to thermal noise. The low temperature can be obtained by the use of dilution refrigerator and electromagnetic shielding. In summary, the ultra-low dissipation and ultra-low operating temperature makes superconducting circuit a favorable platform for quantum computing due to its minimum energy loss and less sensitivity to thermal fluctuations.

2.1.2 Constitutive Relations

Under low temperatures and low voltages, Josephson junctions behave as a pure nonlinear-inductor in parallel with the native parallel-plate capacitor formed by the two superconductor films sandwiching an insulating layer in between. Before we describe the constitutive relations of a Josephson junction, let us start by defining branch flux and the gauge-invariant phase difference. Branch flux is an generalization [18] to the definition of the magnetic flux, as the magnetic flux is only defined for a loop. The branch flux and the branch current of an electric element are given by

$$\Phi(t) = \int_{-\infty}^{t} V(t_1)\, dt_1 \tag{2.1}$$

$$Q(t) = \int_{-\infty}^{t} I(t_1)\, dt_1 \tag{2.2}$$

In the above definitions, the circuit is treated to be at rest at time $t \to -\infty$ with no current or voltage, and all other static fields through in the inductors are regarded as being turned on adiabatically from $t \to -\infty$ to their values at $t = 0$. Using this definition, we can define the inductance of any electric element, even without coils, to be

$$L = \frac{\Phi(t)}{I(t)}. \tag{2.3}$$

From the macroscopic quantum model, the tunneling across the thin insulating layer between the two superconducting islands of a Josephson junction can be modeled by the evanescent overlap of the two superconducting many-electron wave-functions inside the "forbidden" insulating region in the semiclassical limit [35]. The coupled differential equations derived from Schrodinger equations then leads to the DC Josephson current relation, one of the two constitutive relations of Josephson junctions:

$$I(t) = I_0 \sin\left[\frac{2\pi\Phi(t)}{\Phi_0}\right] = I_0 \sin\delta, \tag{2.4}$$

in which $\Phi_0 \equiv= h/(2e)$ is the superconducting flux quantum constant and $\delta \equiv 2\pi\Phi(t)/\Phi_0$ is defined as the gauge-invariant phase difference across the junction. In

the current relation, the periodic flux dependence of the current can be interpreted as being caused by the discreteness of Cooper pair tunneling through the junction. The junction parameter I_0 is called the critical current of the junction, and it scales with the junction area and the inverse of junction thickness. The other constitutive relation, the voltage relation of the Josephson junction, is shown to be [60]

$$V(t) = \frac{\Phi_0}{2\pi}\frac{\mathrm{d}\delta}{\mathrm{d}t} = \varphi_0\frac{\mathrm{d}\delta}{\mathrm{d}t}, \tag{2.5}$$

in which the commonly used constant reduced flux quantum $\varphi_0 = \Phi_0/(2\pi) = \hbar/(2e)$ is introduced to simplify the relation. The two constitute relations altogether describes the dynamics of a Josephson junction and will be utilized in the next part to demonstrate its nonlinear inductance.

2.1.3 Nonlinear Inductance

From the constitutive relations (2.4) and (2.5), we can solve for the expression of the inductance:

$$\begin{aligned} L_J &= V(t)/\left(\frac{\mathrm{d}I(t)}{\mathrm{d}t}\right) = \left(\varphi_0\frac{\mathrm{d}\delta}{\mathrm{d}t}\right)/\left(I_0\cos(\delta)\frac{\mathrm{d}\delta}{\mathrm{d}t}\right) \\ &= \frac{\varphi_0}{I_0\cos(\delta)} = \frac{L_{J0}}{\cos(\delta)}, \end{aligned} \tag{2.6}$$

in which $L_{J0} \equiv \varphi_0/I_0$ is defined as the Josephson effective inductance. Combined with the current relation (2.4), it can be seen that the inductance of a Josephson junction is a nonlinear function of the phase (short for the gauge-invariant phase difference), and hence the current flowing through it. The current-dependent inductance of the Josephson junctions is the heart of superconducting qubits and Josephson-junction-based superconducting parametric amplifiers, as it will become clear in chapter 3. This nonlinear inductive behavior is the manifestation of the inertia of Cooper pairs tunneling across the insulator, which is also known as the kinetic inductance. The other useful parameter of the Josephson junctions is the Josephson energy, the time-

independent portion of the energy stored in a junction, as

$$E(t) = \int_{-\infty}^{t} I\left(t_1\right) V\left(t_1\right) dt_1 = \int_{-\infty}^{t} \left(I_0 \sin\delta\right) \left(\varphi_0 \frac{\mathrm{d}\delta}{\mathrm{d}t}\right) dt_1$$

$$= I_0\varphi_0(1 - \cos\left(\delta\right)) = E_J(1 - \cos\left(\delta\right)) \tag{2.7}$$

$$\Rightarrow \quad E_J = I_0\varphi_0. \tag{2.8}$$

Using (2.7) in the RCSJ model of the Josephson junction [60], the potential energy is then $U = E_J(1 - (I/I_0)\delta - \cos\delta)$, having the shape of a tilted washboard with a corrugation of $2E_J$, as illustrated in Figure 2-1.

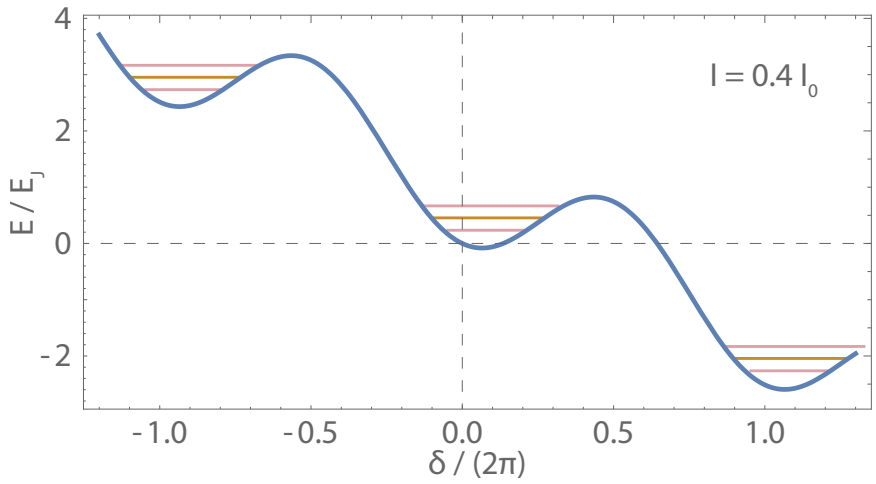

Figure 2-1: Tilted washboard potential of the current-biased Josephson junction with $I = 0.4I_0$. There are can exist bound states at $\delta = n\pi$.

One observation from the current and inductance relations of the Josephson junctions is that there is a one-to-one correspondence between the critical current I_0 and the effective junction inductance L_{J0}. Because the critical current is determined by the physical geometry of the junction, its value is fixed once the device is fabricated. One way to make a tunable Josephson element is to split a junction into two, usually identical, junctions in parallel. The combination of two parallel Josephson junctions is often called a "split Josephson junction" or a SQUID, short for superconducting quantum interference device. It can be shown that the SQUID is equivalent to a

single junction having a tunable critical current. The current relation of a SQUID is

$$I = 2I_0 \cos\left[\pi\left(n - \Phi_{ext}/\Phi_0\right)\right] \sin\delta\varphi, \tag{2.9}$$

in which $\delta\phi$ is defined as the offset phase between the two parallel junctions, and Φ_{ext} is the externally applied magnetic flux. We can see that in this case the effective critical current is now $2I_0 \cos\left[\pi\left(n - \Phi_{ext}/\Phi_0\right)\right]$, which depends on the externally magnetic flux. This is useful, because we can tune the characteristics of the junction "in situ", i.e. during an experiment or measurement.

Another simple way to break the one-to-one correspondence between the critical current and the effective Josephson inductance is to have several Josephson junctions connected in series. For instance, it can be easily shown that the N identical Josephson junctions in series altogether can be treated as one junction having a modified effective Josephson inductance

$$L_{J0} = N\phi_0 I_0. \tag{2.10}$$

2.1.4 Hamiltonian of a Quantum Isolated Josephson Junction

If a Josephson junction is left unconnected from all other elements, it then forms a nonlinear LC resonator. To describe the quantum version of the hamiltonian, we replace the branch flux and branch current by their operators:

$$\Phi \rightarrow \hat{\Phi} \tag{2.11}$$

$$Q \rightarrow \hat{Q} \tag{2.12}$$

$$[\hat{\Phi}, \hat{Q}] = i\hbar. \tag{2.13}$$

The $\hat{Q}$ and $\hat{\Phi}$ can be though of the canonical momentum and coordinate, as can be seen from (2.13). In the special case of Josephson junctions, we further define $\hat{N} \equiv \hat{Q}/(2e)$ to be the number operator representing the number of cooper pairs tunneled through the junction, and $\hat{\theta} \equiv \hat{\Phi}/\varphi_0$ to be the phase operator. The commutation relation of

the charge and phase is then

$$\left[\hat{\theta}, \hat{N}\right] = i. \tag{2.14}$$

In the charge basis, we have [18]

$$\hat{N} = \sum_N N|N\rangle\langle N| \tag{2.15}$$

$$\cos\hat{\theta} = \frac{1}{2}\sum_N (|N\rangle\langle N+1| + |N+\rangle\langle N|), \tag{2.16}$$

and in the phase basis, we have

$$\hat{N} = |\theta\rangle \frac{\partial}{i\partial}\langle\theta|. \tag{2.17}$$

Note that the operator $\hat{N}$ has only integer eigenvalues, whereas the phase $\hat{\theta}$ corresponds to a point on a 2π unit circle. By including the effect of the residual offset charge Q_r on the capacitor (can be the pre-existed charge on the junction capacitor) and discarding the constant term E_J, we can write the Hamiltonian of a Josephson Junction as

$$\begin{aligned} H &= \frac{(\hat{Q} - Qr)^2}{2C_J} + E_J(1 - \cos\hat{\theta}) \\ &\sim \frac{(2e\hat{N} - Qr)^2}{2C_J} - E_J\cos\hat{\theta} \quad (\text{discard } E_J) \\ &= \frac{(2e)^2}{2C_J}(\hat{N} - Qr/(2e))^2 - E_J\cos\hat{\theta} \\ &= E_C\,(N - Q_r/2e)^2 - E_J\cos\theta, \end{aligned} \tag{2.18}$$

in which we define $E_C \equiv (2e)^2/2C_J$ to be the Coulomb charge energy of one Cooper pair. It should be noted that in many references, the charge energy is defined as the Coulomb charge energy of a single electron. The corresponding Hamiltonian in their alternative convention then has an extra factor of four in front of the first term.

Chapter 3

Theory of Josephson Traveling Wave Parametric Amplifiers

3.1 Nonlinear Wave Equation

The derivation of the JTWPA nonlinear wave equation in this section closely follows the procedures of [47] and [48] with slight modifications. Interested readers should be directed to the aforementioned references for further details. The periodically-inserted phase matching resonators are essential for phase matching the degenerate-pump parametric amplification process [47] and will be discussed further in 3.4. However, because these resonators are only weakly coupled to the transmission line and do not affect much the behavior of the system at frequencies outside of the narrow resonance linewidth near the pump tone, it is a fairly good approximation to model the signal dynamics by analyzing the original, resonator-free transmission line and add in the effect of the periodic resonators in the phase mismatch calculation as a perturbation.

Figure 3-1 illustrates the unit cell of the nonlinear transmission line with the presence of the weakly coupled resonators (which we will ignore for now). The Lagrangian of the system, with constant terms omitted, can be written as

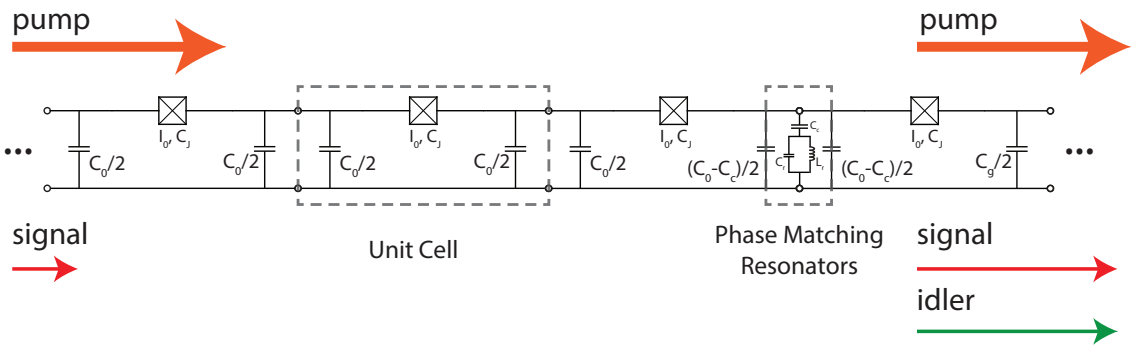

Figure 3-1: The circuit schematic of a resonantly phase matched JTWPA with symmetric unit cell design. Ground capacitors adjacent to the phase matching resonator cell are reduced by half of the coupling capacitance $C_c/2$ each to maintain the same total ground capacitance.

$$L = \sum_{n}^{N} \left[E_J \cos\left(\frac{\phi_{n+1} - \phi_n}{\phi_0}\right) + \frac{C_J}{2}\left(\frac{d\phi_{n+1}}{dt} - \frac{d\phi_n}{dt}\right)^2 + \frac{C_0}{2}\left(\frac{d\phi_n}{dt}\right)^2 \right], \tag{3.1}$$

in which ϕ_n is the node flux at the nth cell, $\phi_0 = \Phi_0/(2\pi)$ is the reduced flux quantum, a is the length of one unit cell, C_0 is the ground capacitance in each unit cell, and $E_J = \phi_0 I_0$ is the Josephson energy, I_0 is the junction critical current, C_J is the junction capacitance, and N is the total number of unit cells. Because the length scale of one unit cell is much smaller than the wavelength of interest, we take the continuum limit of $a \to 0$ and rewrite the above Lagrangian as a spatial integral $L = \int_0^{Na} \mathcal{L} dx$ of the Lagrangian density $\mathcal{L}$ [45]

$$\mathcal{L} = \frac{E_J}{a}\cos\left(\frac{a}{\phi_0}\frac{\partial\phi}{\partial x}\right) + \frac{C_J a}{2}\left(\frac{\partial^2\phi}{\partial t \partial x}\right)^2 + \frac{C_0}{2a}\left(\frac{\partial\phi}{\partial t}\right)^2. \tag{3.2}$$

The Euler-Lagrange equation of (3.2) is in the form

$$\frac{\partial\mathcal{L}}{\partial\phi} = \frac{d}{dx}\left(\frac{\partial\mathcal{L}}{\partial(\partial\phi/\partial x)}\right) + \frac{d}{dt}\left(\frac{\partial\mathcal{L}}{\partial(\partial\phi/\partial t)}\right) - \frac{d^2}{dxdt}\left(\frac{\partial\mathcal{L}}{\partial(\partial^2\phi/\partial x\partial t)}\right). \tag{3.3}$$

Substituting (3.2) into (3.3), we arrive at the exact nonlinear wave equation [48]

$$\frac{aE_J}{\phi_0^2}\cos\left(\frac{a}{\phi_0}\frac{\partial\phi}{\partial x}\right)\frac{\partial^2\phi}{\partial x^2}-\frac{C_0}{a}\frac{\partial^2\phi}{\partial t^2}+C_J a\frac{\partial^4\phi}{\partial t^2\partial x^2}=0. \tag{3.4}$$

Notice that if we taylor expand the cosine term in the exact nonlinear wave equation (3.4) to the first nonlinear order, we will obtain the identical wave equation in [47] and [67, 68]:

$$C_0\frac{\partial^2\phi}{\partial t^2}-\frac{a^2E_J}{\phi_0^2}\frac{\partial^2\phi}{\partial x^2}-C_J a^2\frac{\partial^4\phi}{\partial x^2\partial t^2}+\frac{a^4E_J}{2\phi_0^4}\frac{\partial^2\phi}{\partial x^2}\left(\frac{\partial\phi}{\partial x}\right)^2=0. \tag{3.5}$$

The remainder of this thesis will follow the convention in [48] and work in normalized units. We define the dimensionless node flux, angular frequency, wave vector, position, and time to be

$$\tilde{\phi}=\frac{\phi}{\phi_0},\quad \tilde{\omega}=\frac{2\omega}{\omega_c},\quad \tilde{k}=k\cdot a,\quad \tilde{x}=\frac{x}{a},\quad \text{and}\quad \tilde{t}=\frac{t}{\tau_c}=\frac{\omega_c}{2}t \tag{3.6}$$

respectively, in which $\omega_c=(2/\phi_0)\sqrt{E_J/C_0}=2/\sqrt{L_JC_0}$ is the cut-off frequency of the nominal dispersionless transmission line ($C_J=0$). Finally, define the normalized dispersion parameter $\beta=C_J/C_0$ and drop the tildes for convenience, we arrive at the normalized nonlinear wave equation

$$\phi_{xx}-\phi_{\mathrm{tt}}+\beta\phi_{\mathrm{xxtt}}=\frac{1}{2}\phi_{\mathrm{xx}}\phi_x^2, \tag{3.7}$$

in which we adopt the short-hand notations for the partial derivatives $\phi_{x_i}=\partial\phi/\partial x_i$, $\phi_{x_ix_j}=\partial^2\phi/\partial x_i\partial x_j$, and so forth. The terms on the left-hand side of (3.7) are all linear with respect to ϕ and hence characterize the dispersion of the transmission line, whereas the nonlinear term on the right-hand side is in cubic order of ϕ and mediates four-wave mixing processes.

3.2 Hamiltonian

For completeness, we present here the quantum treatment of JTWPA following the derivation in [22] with modifications. We will first expand the nonlinear term to

fourth order, and then convert the Lagrangian density $\mathcal{L}$ in (3.2) to normalized units:

$$L = \int_0^{Na} \mathcal{L} dx = \int_0^N \mathcal{L} * a d\tilde{x} = \int_0^N \tilde{\mathcal{L}} d\tilde{x}, \quad \text{(dropping tildes from now on)} \tag{3.8}$$

$$\begin{aligned}\tilde{\mathcal{L}} &\approx E_J \left(-\frac{1}{2} \left(\frac{a}{\phi_0} \phi_x \right)^2 + \frac{1}{24} \left(\frac{a}{\phi_0} \phi_x \right)^4 \right) + \frac{C_J a}{2} \phi_{xt}^2 + \frac{C_0}{2a} \phi_t^2 \\ &= E_J \left(-\frac{1}{2} \tilde{\phi}_{\tilde{x}}^2 + \frac{1}{24} \tilde{\phi}_{\tilde{x}}^4 \right) + \frac{C_J a}{2} \frac{\phi_0^2}{a^2 L_J C_0} \tilde{\phi}_{\tilde{x}\tilde{t}}^2 + \frac{C_0}{2a} \frac{\phi_0^2}{L_J C_0} \tilde{\phi}_{\tilde{t}}^2 \qquad (3.9) \\ &= \frac{E_J}{2} \left(-\phi_x^2 + \frac{1}{12} \phi_x^4 + \beta \phi_{xt}^2 + \phi_t^2 \right) = \mathcal{L}. \qquad (3.10)\end{aligned}$$

Again, we dropped all the tildes from (3.9) to (3.10) for notation convenience.

Using $\phi(x,t)$ as the canonical momentum, we can express the canonical momentum $\pi(x,t)$ as

$$\pi(x,t) = \frac{\delta \mathcal{L}}{\delta \phi_t} = \frac{\partial \mathcal{L}}{\partial \phi_t} - \frac{\partial}{\partial x} \frac{\partial \mathcal{L}}{\partial \phi_{xt}} = E_J(\phi_t - \beta \phi_{xxt}). \tag{3.11}$$

Using integration by parts and dropping the produced constant boundary terms, we arrive at the Hamiltonian

$$H = \int_0^N dx \mathcal{H} = \int_0^N dx (\pi \phi_t - \mathcal{L}) = \frac{E_J}{2} \int_0^N dx \left(\phi_t^2 + \phi_x^2 + \beta \phi_{xt}^2 - \frac{1}{12} \phi_x^4 \right). \tag{3.12}$$

Before we quantize the Hamiltonian, we introduce the normalized Hamiltonian density $\tilde{H}_0$ and $\tilde{H}_1$ to be

$$\tilde{\mathcal{H}}_0 = \phi_t^2 + \phi_x^2 + \beta \phi_{xt}^2, \quad \text{and} \quad \tilde{\mathcal{H}}_1 = -\frac{1}{12} \phi_x^4 \tag{3.13}$$

respectively, and they satisfy the relation $\mathcal{H} = (E_J/(2))\tilde{\mathcal{H}} = (E_J/(2))(\tilde{\mathcal{H}}_0 + \tilde{\mathcal{H}}_1)$. The physical interpretation of $\tilde{\mathcal{H}}_1$ and $\tilde{\mathcal{H}}_2$ is straightforward: they are the linear and nonlinear Hamiltonian density of the JTWPA that are normalized to photon numbers.

We are now ready to quantize the Hamiltonian with the above definitions. Treating the nonlinear term as perturbation, we will use express the whole Hamiltonian in the normal basis of $\tilde{\mathcal{H}}_0$ [22]. The fields $\phi(x,t)$, $\pi(x,t)$ are promoted to operators $\hat{\phi}(x,t)$, $\hat{\pi}(x,t)$ respectively, and the canonical operators obey the commutation relation

$$\left[\hat{\phi}(x,t), \hat{\pi}(x',t)\right] = i\hbar\delta(x-x'). \tag{3.14}$$

With the definitions of $Z_0 = \sqrt{L_J}C_0$, $k(\omega) = \omega/\sqrt{1-\beta\omega^2} = n(\omega)\omega$, and $E_J = \hbar\omega_J$, the operator (normalized) $\hat{\phi}(x,t)$ can be expressed as [57]

$$\hat{\phi}(x,t) = \frac{1}{\phi_0}\int_0^\infty \frac{1}{\sqrt{2\pi}} d\left(\omega\frac{\omega_c}{2}\right)\sqrt{\frac{\hbar Z_0 * n(\omega)}{2\omega\omega_c/2}} e^{-jkx}\hat{a}_\omega e^{j\omega t} + H.c. \tag{3.15}$$

$$= \int_0^\infty d\omega \sqrt{\frac{n(\omega)\omega_c^2}{16\pi\omega\omega_J}}\hat{a}_\omega e^{j(\omega t - kx)} + H.c., \tag{3.16}$$

in which $H.c.$ standards for the Hermitian conjugate of the preceding term, and the annihilation operator $\hat{a}_\omega$ satisfies the standard commutation relation

$$\left[\hat{a}_\omega, \hat{a}^\dagger_{\omega'}\right] = i\delta(\omega,\omega'). \tag{3.17}$$

Similarly, the operator $\hat{\pi}(x,t)$, from (3.16) and (3.11), can be written in terms of creation and annihilation operators as

$$\hat{\pi}(x,t) = \left((j\omega E_J)(1-\beta k^2)\right)\int_0^\infty d\omega \sqrt{\frac{n(\omega)\omega_c^2}{16\pi\omega\omega_J}}\hat{a}_\omega e^{j(\omega t - kx)} + H.c. \tag{3.18}$$

$$= jE_J\int_0^\infty d\omega\ n(\omega)^2\sqrt{\frac{n(\omega)\omega\omega_c^2}{16\pi\omega_J}}\hat{a}_\omega e^{j(\omega t - kx)} + H.c.. \tag{3.19}$$

Following the derivations in [22], the physical Hamiltonian $H_0 = (E_J/2)\int_0^N dx\tilde{H}_0$ becomes (after dropping the constant zero point energy terms)

$$H_0 = \int_0^\infty d\omega\hbar\omega\hat{a}^\dagger_\omega\hat{a}_\omega. \tag{3.20}$$

Notice that in (3.20) (only) we used back the physical ω for clarity. Finally. tHe nonlinear Hamiltonian $H_1 = (E_J/2)\int_0^N dx\tilde{H}_1$ can be expressed in the normal basis using (3.16) and (3.19). Note that the integral in frequency in (3.20) is only strictly valid in the continuum limit of $a \Rightarrow 0$. When a has a finite size (and N becomes finite), the propagation modes therefore do not span the entire continuous frequency

spectrum [22, 57].

3.3 Equations of Motion

The equations of motion for the classical and quantum field operator can be derived from the nonlinear wave equation (3.7) and the Heisenberg equations of motion respectively, and the resulting evolution for both the classical and quantum operators are shown to be the same [42]. The quantum nature of the system is manifested in the non-zero commutation relation of the operators and results in additional quantum noise. We will therefore use the classical nonlinear wave equation to derive the evolution dynamics of the amplifier and apply the treatment of [42] to account for the quantum noise in the end.

The traveling wave ansatz commonly used in JTWPA analyses [47] is

$$\phi(x,t) = \frac{1}{2}\left(A_p(x)e^{i(k_p x+\omega_p t)} + A_s(x)e^{i(k_s x+\omega_s t)} + A_i(x)e^{i(k_i x+\omega_i t)}\right) + c.c., \tag{3.21}$$

in which A_m, k_m, ω_m are the frequency, wave vector, and flux amplitude of wave m respectively, with $m \in \{p, s, i\}$ representing the pump, signal, and idler. *c.c.* represents the complex conjugate of its immediate preceding term [10, 2]. One can then substitute the ansatz (3.21) into the nonlinear wave equation (3.7) and solve for the evolution of the degenerate-pump parametric amplification process $2\omega_p \rightarrow \omega_s + \omega_i$. Instead of going into the details of the mathematical manipulations and simplifications, we will highlight the important approximations made in the standard derivation and present the final, simplified coupled mode equations. Nonetheless, the descriptions of these noted approximations will still shed lights on the high level procedures of the detailed derivation. The main approximations are as follows:

1. For each wave component, only the terms oscillating at the same frequency from the wave equation are kept in its evolution equation, and the effects of the other fast oscillating (or off-resonant) terms are neglected. This approximation

is equivalent to standard the rotating wave approximation (RWA) in quantum optics and atomic physics.

2. For wave components whose frequencies are much lower than the cut-off frequency of the transmission line, its dispersion relation can be well approximated by the linear portion of (3.7) (the nonlinear term on the right-hand side is omitted in solving linear dispersion). This is often recognized as the continuum-limit approximation in sold state physics.

3. The pump tone is a strong, coherent state whose dynamics are negligibly affected by the introduction of the weak signal and idlers. Therefore, the intensity of the pump tone is assumed to remain constant and classical in the entire process. This is termed the stiff-pump approximation [20].

4. The field envelopes A_m are assumed to be slowly varying. More specifically, $\frac{\partial^2 A_j}{\partial x^2} \ll k_j \frac{\partial A_j}{\partial x}$ and $\frac{\partial^2 A_j}{\partial x^2} \ll k_j \frac{\partial A_j}{\partial x}$, and these higher order derivatives are neglected in the evolution equations. This is commonly referred to as the slowly varying envelope approximation (SVEA) in the context of nonlinear optics [10, 2].

The validities of the aforementioned approximations will be carefully evaluated and in some cases relaxed throughout this thesis. Finally, the simplified equations of motion for the degenerate-pump parametric amplification process in the rotating frame ($A_{sr}(x) = A_s(x)e^{-j\alpha_s x}$, $A_{ir}(x) = A_i(x)e^{-j\alpha_i x}$) are

$$\begin{aligned} \frac{\mathrm{d}A_{sr}(x)}{\mathrm{d}x} &= j\kappa_s A_{ir}^*(x)e^{j\Delta_k x}, \quad \text{and} \\ \frac{\mathrm{d}A_{ir}^*(x)}{\mathrm{d}x} &= -j\kappa_i A_{sr}(x)e^{-j\Delta_k x}. \end{aligned} \tag{3.22}$$

The symbols introduced in (3.22) are defined as follows:

$$\alpha_s = \frac{k_s^3 k_p^2 |A_p(x)|^2}{8\omega_s^2}, \qquad \alpha_i = \frac{k_i^3 k_p^2 |A_p(x)|^2}{8\omega_i^2}, \qquad \alpha_p = \frac{k_p^3 k_p^2 |A_p(x)|^2}{16\omega_p^2} \tag{3.23}$$

$$\Delta k_l = 2k_p - k_s - k_i, \qquad \Delta k_{nl} = 2\alpha_p - \alpha_s - \alpha_i, \qquad \Delta k = \Delta k_l + \Delta k_{nl}, \tag{3.24}$$

$$\kappa_s = \frac{k_s k_i k_p^2 (k_i + \Delta k_l) |A_p(x)|^2}{16\omega_s^2}, \qquad \kappa_i = \frac{k_s k_i k_p^2 (k_s + \Delta k_l) |A_p(x)|^2}{16\omega_i^2}. \tag{3.25}$$

Each of the above definitions has a clear physical interpretation. α_s and α_i are the pump-induced cross-phase modulation (XPM) terms that signal and idler experience respectively, and α_p is the self-phase modulation (SPM) the classical pump experiences itself. Δk_l is the net linear phase mismatch originated from dispersion, Δk_{nl} is the net nonlinear phase modulation resulted from the Kerr effect, and Δk is the total effective phase mismatch accounting for both the linear and nonlinear contributions. Finally, κ_s and κ_i are the corresponding coupling strength of the signal and idler flux.

3.4 Phase Matching

The phase matching condition, signifying momentum conservation, is crucial to the overall performance of a nonlinear parametric amplifier of any kind. Whereas a properly phase matched parametric amplifier exhibits exponential gain with respect to its device length, a poorly phased matched amplifier could only achieve gain in quadratic order and has a much shorter coherence length [10]. For this reason, TWPAs based on Josephson junctions preceding the resonantly phased matched JTWPA [47, 38] have not demonstrated sufficient gain to replace existing semiconductor amplifier technology.

Without any deliberate phase matching scheme, the four-wave parametric amplification process for a typical Josephson transmission line with normal dispersion is poorly phase mismatched. This is because for a degenerate-pump four-wave parametric amplifier, the intrinsic linear phase mismatch Δk_l from normal dispersion and the nonlinear phase mismatch Δk_{nl} from the Josephson junction nonlinearity are of

the same sign (negative), and hence they altogether makes phase matching condition even worse. Moreover, it is usually desirable to use a high pump power to improve the parametric gain because the coupling strength is proportional to the input pump power. However, an increased input pump power also results in a larger nonlinear phase mismatch which reduces the gain. The trade-off between the coupling strength and the phase mismatch ultimately limits the maximal gain achievable in a non-phase matched amplifier.

The weakly coupled resonators are introduced in [47, 38] to phase match the parametric amplification process. As previously mentioned, these weakly coupled phase matching resonators introduce a weak resonance near the pump frequency. When properly placed, this dispersion feature would result in a small increase in the pump wave vector which in turn compensates for the negative phase mismatch in the unperturbed case. Figure 3-2 illustrates the effect of the periodically coupled resonators on the phase matching condition. In the frequency range of interest (5-8 GHz), although the intrinsic linear mismatch on an unperturbed transmission line is small, the overall phase mismatch is dominated by the non-negligible nonlinear mismatch. The nonlinear phase mismatch is usually significant at a typical pump power level and therefore impedes exponential gain. In the resonant phase matching (RPM) scheme, the wave vector of the pump is noticeably increased from its unperturbed value, whereas those of the signal and idler are minimally affected. Overall the linear phase mismatch increases and is enough to cancel out the negative nonlinear mismatch caused by the pump. Experimentally one can adjust the pump power and slightly tune the pump frequency near the resonance to find the optimal configuration in situ.

Although the RPM JTWPAs have become mainstream in superconducting quantum experiments and is the main object of discussion in this thesis, it is worth mentioning that amplifiers using alternative phase matching schemes such as periodic loading [28] and photonic bandgap [50] have also been explored and demonstrated. Regardless of the specific implementation, these phase matching schemes all rely on the high-level idea of increasing the intrinsic linear mismatch by dispersion engineering to compensate for the always-on nonlinear mismatch.

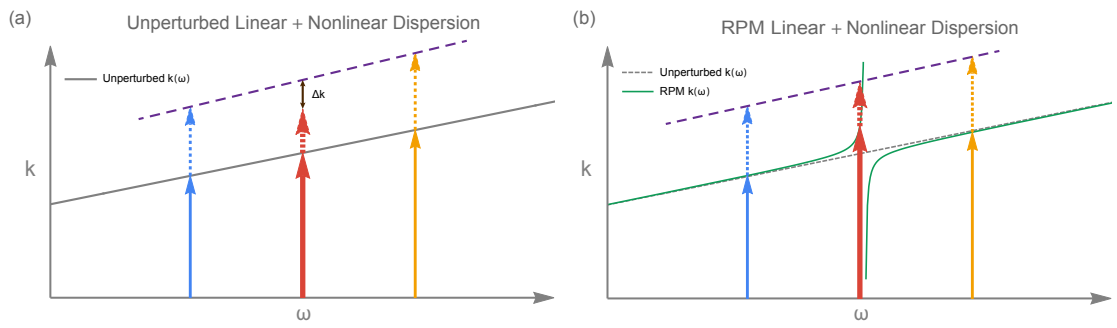

Figure 3-2: Pictorial illustration of the phase matching condition on an unperturbed transmission line (a) and a transmission line with weakly coupled resonators (b). The dispersion relation of the unperturbed transmission line is colored in gray in both (a) and (b), and the dispersion relation of the RPM transmission line is colored in green in (b). The wave vectors and nonlinear modulations of the signal, idler, and pump are colored in blue, orange, and red respectively. The solid and dashed arrows represent the linear and nonlinear components of the effective wave vectors respectively. The perfect phase matching condition is obtained in (b) for the RPM scheme as the tips of all the wave components fall onto the same line (dashed and in purple in this figure).

3.5 Performance

Figure 3-3 shows the simulated gain and phase mismatch spectrum of a resonantly phase-matched JTWPA and a non-matched JTWPA at pump frequency $\omega_p/(2\pi) =$ 5.97GHz and pump current $I_p = 0.5I_0$ [47]. The resonantly phase-matched design is shown to have much higher gain and broader bandwidth than the non-matched one because of the better phase matching condition.

Here, we summarize the experimental results of the demonstration of a resonantly phase-matched JTWPA in [38]. Figure 3-4 (a) shows the measured and fitted signal gain and phase-mismatch as a function of pump power at 6.584 GHz. The phase mismatch Δk is shown for a pump at 7.157 GHz (solid green, "RPM") and at 6.5 GHz (solid purple, "detuned"). The theoretically predicted values for both the Δk

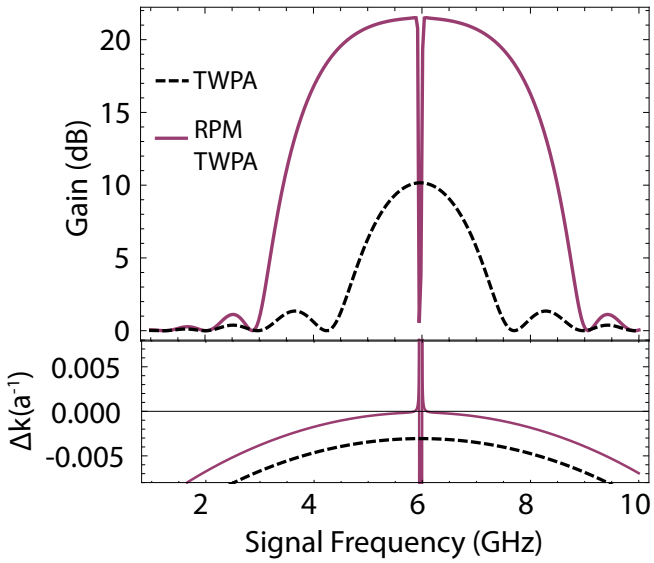

Figure 3-3: Gain and phase mismatch of the resonantly phase-matched JTWPA (purple) and the non-matched JTWPA (black dashed) as a function of signal frequency with $\omega_p/(2\pi) = 5.97GHz$ and $I_p = 0.5I_0$. Figure reproduced from [47].

and gain agrees well with the measured values, except at higher pump current where the measured gain slumps. A plausible cause of this drop of gain at high pump current is the drop in pump transmission for pump currents near the junction critical current [38]. Figure 3-4 (b) shows the measured gain bandwidth profile of the fabricated device at a high pump current $I_p = 0.91I_0$ at 7.157 GHz. This represents the most general-purpose operating configuration, with 20 dB gain with a bandwidth of over 3 GHz. The small ripples in the measured gain are likely caused by imperfect impedance matching between the JTWPA and 50 Ω connectors.

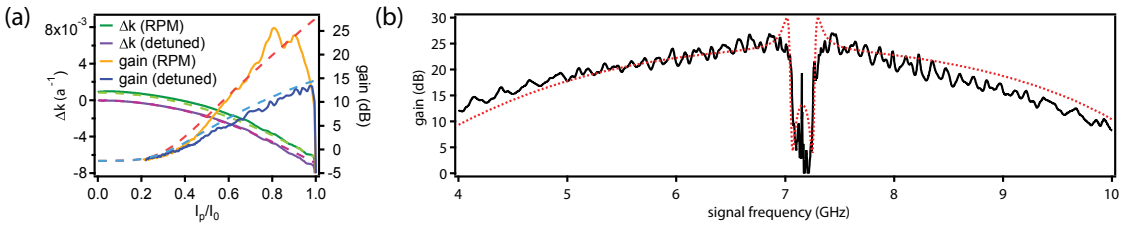

Figure 3-4: (a) Measured (solid) and predicted (dashed) phase mismatch and gain versus pump power at signal frequency 6.584 GHz. (b) Measured (solid) and fitted (dashed) gain profile of the JTWPA at a strong pump at frequency 7.157GHz and a current level $I_p = 0.91I_0$. Figure reproduced from [38].

The overall system noise was extracted to be $9.01 \pm 0.23K$ and $602 \pm 15mK$ when the pump of the JTWPA was put to off and on respectively [38]. This corresponded to a quantum efficiency of $\eta = 0.48 \pm 0.016$. With the insertion loss between the cavity and JTWPA ($\eta_L = 0.69$), distributed loss in the JTWPA ($\eta_D = 0.9$), and the finite gain of the JTWPA relative to the high electron mobility transistor amplifier (HEMT) ($\eta_H = 0.93$), the intrinsic quantum efficiency of the JTWPA was calculated to be 0.75 including the unaccounted quantum efficiency reduction.

In summary, in past experiments, JTWPAs have achieved a gain larger than 20 dB over a 3 GHz-bandwidth. The saturation power at 1 dB compression point is measured to be -99 dBm. The overall system noise when the pump of the JTWPA was $602 \pm 15mK$, corresponding to a near-quantum-limited noise performance. The overall system quantum efficiency was 0.49 and the intrinsic quantum efficiency of the JTWPA was extracted to be 0.75. Understanding this imperfect quantum efficiency by moving beyond the model described in this chapter is the topic of the next chapter.

Chapter 4

Multi-Mode Dynamics of JTWPAs

4.1 Introduction

JTPWAs have become the workhorse amplifier for a wide variety of microwave superconducting quantum experiments [24, 64, 43, 27, 15] since its demonstration in 2015 [47, 38]. In particular, their increasing popularity in superconducting quantum computing is due to their high dynamic range (∼100dBm), GHz simultaneous bandwidth, and near quantum limited noise performance, which altogether allow for simultaneous readout for more than 20 qubits. The quantum efficiency of the readout chain is an important metric as it directly affects the speed and fidelity of qubit readout. The intrinsic quantum efficiency of a typical JTWPA is experimentally extracted to be 75% [38], taking into account the distributed loss contribution of 90%. This means there is an unaccounted inefficiency of about 83% in amplifier operation. The two-mode coupled mode theory model presented in section 3.3, despite its success in designing JTWPAs, describes an ideal two-mode parametric amplifier and hence does not yield any insight into the quantum efficiency of an actual device. In this chapter, we will discuss the non-idealities of JTWPAs in more details, present a multi-mode coupled mode theory model, and finally use this model to reproduce the experimentally observed quantum efficiency.

4.2 Third Harmonic Generation of the Pump

As previously mentioned, the stiff-pump approximation is used to derive the simplified two-mode model (3.22). Specifically, the amplitude of the pump is assumed to be constant across the entire device if the dielectric loss is neglected. While it is true that the influence of the signal dynamics on the pump is negligible below the gain compression point, the pump is nevertheless never constant in practice. Besides the desired parametric amplification process, the nonlinearity of the Josephson junctions will also simultaneously mediate all other four-wave mixing processes possible, including third-harmonic generation (THG) from the pump [4].

If the THG process of the pump is not extremely phase mismatched, the amount of pump power transferred to the third harmonics will be non-trivial, and the pump power will consequently be spatially modulated. In fact, THG of the pump has already been shown to cause a number of issues in TWPAs, including gain reduction, dynamic range reduction, and the introduction of other harmonics [28, 66, 19]. To more accurately predict the gain and subsequently the quantum efficiency of the JTWPA, we propose to incorporate the effect of the THG as an amplitude modulation of the pump. However, we will still use the stiff-pump approximation in the sense that the dynamics of the pump is only affected by the THG but not by the signal and idlers. This can be simply justified by the fact that we can always choose to work with a weaker input signal at the expense of a weaker claim on the dynamic range.

To analyze the dynamics of the THG of the pump, we use instead the traveling wave ansatz

$$\phi(x,t) = A_{p1}(x)e^{j(\omega_p t + k_{p1}x)} + A_{p2}(x)e^{j(3\omega_p t + k_{p2}x)} + c.c., \tag{4.1}$$

in which we use the subscript index $m = 1, 2$ to denote the pump and its third harmonics respectively for notational convenience. A_{pm}, k_{pm}, ω_{pm} are the normalized complex flux amplitude, linear wave vector, and angular frequency of the wave m respectively. In particular, we have $\omega_{p2} = 3\omega_{p1}$ in this notation, and pump 1 is the same as the original pump defined in section 3.3. Substituting (4.1) into (3.7) and

applying SVEA, we arrive at the equations of motion as

$$\begin{aligned} A'_{p1}(x) &= j\tilde{\alpha}_{p1}(x)A_{p1}(x) + je^{j\Delta k_{l,\mathrm{THG}}x}\kappa_{p1}A^*_{p1}(x)^2A_{p2}(x) \\ A'_{p2}(x) &= j\tilde{\alpha}_{p2}(x)A_{p2}(x) + je^{-j\Delta k_{l,\mathrm{THG}}x}\kappa_{p2}A_{p1}(x)^3, \end{aligned} \tag{4.2}$$

in which $\Delta k_{l,\mathrm{THG}}$, $\tilde{\alpha_{pm}}$, and κ_{pm} defined similarly as

$$\Delta k_{l,\mathrm{THG}} = (k_{p2} - 3k_{p1}), \tag{4.3}$$

$$\tilde{\alpha}_{p1}(x) = \frac{k_{p1}^3}{16\omega_{p1}^2}\left(k_{p1}^2|A_{p1}(x)|^2 + 2k_{p2}^2|A_{p2}(x)|^2\right), \tag{4.4}$$

$$\alpha_{p2}(x) = \frac{k_{p1}^3}{16\omega_{p1}^2}\left(2k_{p1}^2|A_{p1}(x)|^2 + k_{p2}^2|A_{p2}(x)|^2\right). \tag{4.5}$$

$\Delta k_{l,\mathrm{THG}}$ is the linear phase mismatch at position x, and $\tilde{\alpha}_{p1}(x)$, $\tilde{\alpha}_{p2}(x)$ can be understood as the instantaneous phase modulation terms of the pump and its third harmonics respectively.

The equations of motion (4.2) can be solved either analytically in terms of elliptical integrals of the first kind [53] or numerically using modern differential solvers. With the experimentally extracted parameters of [38], we numerically solve for the THG dynamics and plot the power and normalized current of the two wave components in figure 4-1.

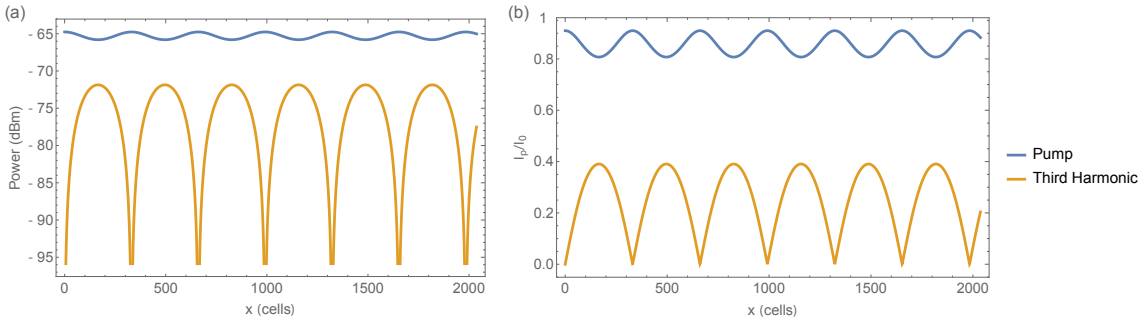

Figure 4-1: Dynamics of the pump (blue) and its third harmonic (orange) in (a) power and (b) normalized current with an initial input pump current of $I_p(0) = 0.91I_0$. The currents of the pump and its third harmonic in (b) are normalized to the critical current of the Josephson junctions.

Figure 4-1 clearly shows that the spatial modulation of the pump power from THG is far from trivial: the power of the third harmonics becomes only 6dBm lower than that of the pump at periodic peaks. Several consequences arise from the THG dynamics of the pump. First, both the phase mismatch and the coupling strength of the parametric amplification becomes spatially varying due to their pump power dependence. Because the gain dependence on phase mismatch and coupling strength is exponential, one has to incorporate the spatial modulation into the model to predict the gain accurately. Second, the spatial modulation of the pump power itself also introduces an addition phase mismatch originated from the periodicity of the modulation. This additional phase mismatch therefore needs to be accounted in the model as well, because it affects the overall effective phase mismatch of the parametric amplification everywhere across the device. Third, the generated third harmonics can also help mediate the same parametric amplification through the down-conversion process $\gamma_{\omega_{p2}} \rightarrow \gamma_{\omega_{p1}} + \gamma_{\omega_s} + \gamma_{\omega_i}$, in which γ_{ω_m} denotes a photon at frequency ω_m. Depending on the relative phase between the third harmonics of the pump, the third harmonics will either boost or suppress the parametric amplification. To properly include the contribution of the third harmonics to the signal dynamics, we will model the third harmonic as an effective second pump, as already hinted by our

use of subscript $p2$ in notation. Finally, the inclusion of third harmonics requires a change in the pump current, which will be discussed further next.

4.3 Pump Current Normalization

Compared to the linearized signal parametric amplification process, the THG process of the pump is purely nonlinear and the pump evolution is very sensitive to the initial condition. The normalized pump current used in [38] is determined to be $I_{p1n}(x = 0) = I_{p1}(0)/I_0 = 0.91$. This number is extracted as the ratio r_n of the pump power used during device operation and the critical pump power at which the Josephson junctions start to exit the superconducting state. This method will produce a reasonable approximation of the true normalized pump current if the pump stays constant across the entire device. However, its deduced value will deviate rapidly from the actual value when the power at the third harmonics becomes significant. Indeed, if the initial normalized pump current is truly 0.91, we see from figure 4-1 that the total normalized current would become as large as $\max(|I_{pn,\mathrm{tot}}(x)|) = \max(|I_{p1n}(x) + I_{p2n}(x)|) \approx 1.174$, which far exceeds the critical current threshold. Clearly an initial pump current of $0.91I_0$ is unphysical when we take into account the third harmonics. The total current fluctuates even when the total power is conserved because the characteristic impedance at the frequencies of the pump and the third harmonic are different. Consequently, the initial input pump current needs to be properly normalized to closely approximate the pump evolution.

Here we propose a simple, iterative method of approximating the actual initial pump current. Neglecting momentarily the constraint that the total normalized current going through a Josephson junction has to be less than unity, we first set the initial lower and upper bound of the normalize pump current to be 0 and 1 respectively and pick a reasonable initial guess in between to start with. Using the current initial condition for the pump, we can numerically solve (4.2), extract the peak total current within the device, and then compare it with the threshold 1. If the difference between simulated peak normalized current and unity is less than the desired tolerance, we

declare r_n of the present trial value to be the desired initial condition. Otherwise, we update the upper/lower bound of the range to be the present trial value if the peak normalized total current is less/larger than unity. We then choose the middle value of the updated range as the new initial condition and numerically compute the maximum normalized total current again. We keep repeating the bisection process until a satisfactory approximation is found. Using this procedure, we calculate the proper initial pump current $I_{p1n}(0)$ to be around $0.78 \cdot 0.91 \approx 0.71$. As will be shown later, this adjusted pump initial condition will yield both a more realistic gain dynamics and a quantum efficiency closer to the experimentally determined value.

It is important to note, however, that the value calculated by the aforementioned iterative method on (4.2) is still not exact but a reasonable enough approximation of the true pump condition. One shortcoming of the simple model (4.2) is that it does not capture the effects from the other harmonics of the pump. For instance, $\gamma_{9\omega_p} \leftarrow 3\gamma_{3\omega_p}$ can be in turn generated from the third harmonic through THG, and $\gamma_{5\omega_p} \leftarrow 2\gamma_{3\omega_p} - \gamma\omega_p$ can be generated from the scattering of one pump photon and two third harmonic photons. Because the phase mismatch of processes involving higher frequency component(s) is even larger, and the coupling strength of any four-wave mixing scales with the intensity of the interacting waves, these additional nonlinear processes are fortunately much weaker than the primary THG of the pump. Consequently, the two-mode model of (4.2) can approximate the pump dynamics to a very good extent. Nevertheless, if an initial condition with better precision is desired, one can use the harmonic balance method [49] to obtain a better estimation using modern microwave simulation softwares such as LTspice [21] and Microwave Office [62].

In addition, the dielectric loss of the transmission line also slightly increases the critical input pump current at which the breakdown of superconductivity happens precisely. Intuitively, when both the pump and the third harmonics get attenuated as they propagate down the device, the total normalized current will peak at a value lower than that of its lossless counterpart. This means more initial pump current is required to reach the critical current at the presence of loss. One can utilize the beam splitter loss model [13] to incorporate small propagation loss by introducing decay

terms into the lossless coupled mode equations (4.2):

$$\begin{aligned} A'_{p1}(x) + \frac{k_{p1i}}{2} A_{p1r}(x) &= j\tilde{\alpha}_{p1}(x) A_{p1}(x) + j e^{j\Delta k_{l,\mathrm{THG}} x} \kappa_{p1} A^*_{p1}(x)^2 A_{p2}(x) \\ A'_{p2}(x) + \frac{k_{p2i}}{2} A_{p2r}(x) &= j\tilde{\alpha}_{p2}(x) A_{p2}(x) + j e^{-j\Delta k_{l,\mathrm{THG}} x} \kappa_{p2} A_{p1}(x)^3, \end{aligned} \tag{4.6}$$

in which k_{p1i} and k_{p2i} are the imaginary components of the wave vectors introduced to model the dielectric loss. Indeed, using the loss tangents of 0.027 and 0.034 for the (high power) pump and its third harmonic respectively [38], we obtain a ~ 0.01 increase in the normalized critical input pump current, equivalent to $< 2\%$ of the original estimate. Although the correction to the pump initial condition from propagation loss is small, (4.6) serves as an important tool for modeling the pump attenuation effect due to dielectric loss[38]. Figure 4-2 compares the pump dynamics with and without attenuation as a function of position x with normalized initial pump current $I_{p1n} = 0.78 \cdot 0.91 = 0.71$ and loss tangent $\tan(\delta) = 0.027$ [38]. It is clear from figure 4-2 that the third harmonic is still non-negligible at the presence with attenuation.

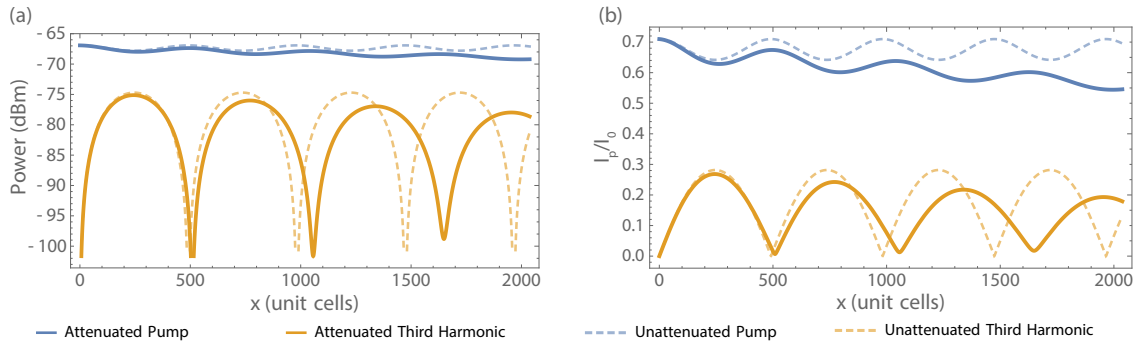

Figure 4-2: Dynamics of the pump (blue) and its third harmonic (orange) in (a) power and (b) normalized current with an initial input pump current of $I_p(0) = 0.78 \cdot 0.91 I_0 = 0.71 I_0$. Solid and dashed lines represent the wave evolution with and without material loss respectively. The currents of the pump and its third harmonic plotted in (b) are normalized to the critical current of the Josephson junctions.

Finally, another source of uncertainty in the pump initial condition comes from the confounding effect of THG on characterizing the dielectric loss at high pump power. This is because the two level system (TLS) loss become saturated at high power and is shown to differ much from its low-power value [38], and so the dielectric loss of the pump is characterized at high pump power and unavoidably subject to stronger nonlinear processes. To obtain a more accurate loss tangent value, one can either fabricate and characterize a linear test structure on the same mask for material loss, or measure the actual nonlinear device at various pump power and optimize both the loss tangent and the initial pump power together to best fit the loss measurement set.

4.4 Quantum Many-Mode Processes

Similar to the generation of other pump harmonics, a full chain of signal and idler sidebands exist and are generated through different four-wave mixing processes. For instance, signal and idler too can generate their respective third harmonics through $3\gamma_{\omega_m} \rightarrow \gamma_{\omega_m}$, and higher order signal and idlers can be generated through the cascaded frequency conversion processes $\gamma_{\omega_m} + 2\gamma_{\omega_p} \rightarrow \gamma_{\omega_m+2\omega_p}$. In this thesis, we will refer to all the signal sidebands as idlers and assign each an index to differentiate them from each other. The main idler is chosen to have index 1. With the same argument presented in section 4.3 and that the typical input signal power is several orders of magnitude weaker than the input pump power, only processes involving exactly two pump photons are significant to the overall system dynamics and worth careful considerations. Figure 4-3 illustrates a selection of the signal sidebands that are generated through two-pump-photon processes. Treating the third harmonic of the pump as an effective second pump, we can categorize all the nonlinear processes into two main categories: parametric amplification and frequency conversion (or Bragg scattering).

The parametric amplification processes include both degenerate and non-degenerate pump processes. Degenerate pump parametric amplification processes include the main process $2\gamma_{\omega_{p1}} \rightarrow \gamma_{\omega_s} + \gamma_{\omega_{i1}}$ and the third harmonic assisted process $2\gamma_{\omega_{p2}} \rightarrow$

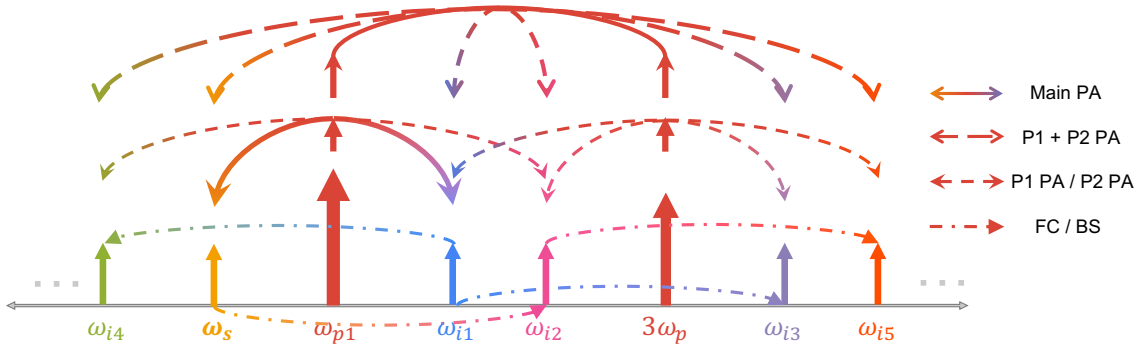

Figure 4-3: Graphical illustration of the many mode processes through degenerate or non-degenerate pump four-wave mixing. The main parametric amplification process of interest is indicated by the solid, orange-to-blue gradient arrow. Dashed arrows represent degenerate and non-degenerate pump parametric amplification processes. Dashed-dotted arrows represent frequency conversion or bragg scattering processes. Here, the cascaded frequency conversion processes of the main signal and idler (ω_{i1}) are represented by $\omega_s \rightarrow \omega_{i2}$ and $\omega_i \rightarrow \omega_{i3}$ respectively.

$\gamma_{\omega_{i1}} + \gamma_{\omega_{i5}}$. Non-degenerate parametric amplification processes include the generation of ω_{i3} and ω_{i5} through $\gamma_{\omega_{p1}} + \gamma_{\omega_{p2}} \rightarrow \gamma_{\omega_s} + \gamma_{\omega_{i3}}$ and $\gamma_{\omega_{p1}} + \gamma_{\omega_{p2}} \rightarrow \gamma_{\omega_{i4}} + \gamma_{\omega_{i5}}$ respectively.

The frequency conversion/Bragg scattering processes include the generation of higher order signal and idler through $\gamma_{\omega_s} + 2\gamma_{\omega_{p1}} \rightarrow \gamma_{\omega_{i2}}$ and $\gamma_{\omega_{i1}} + 2\gamma_{\omega_{p1}} \rightarrow \gamma_{\omega_{i3}}$ respectively. They are dubbed the cascaded frequency conversion processes because they can again frequency up-convert the generated sidebands into even higher frequency images in the same fashion. For instance, ω_{i5} can be generated from the signal through two frequency conversions $\gamma_{\omega_s} \rightarrow \gamma_{\omega_{i2}} \rightarrow \gamma_{\omega_{i5}}$ in series, each mediated by a pair of degenerate pump photons. Moreover, frequency conversion processes also include processes involving the scattering of two non-degenerate pump photons. For instance, a ω_{i2} photon can also be generated via $\gamma_{\omega_s} + \gamma_{\omega_{p2}} \rightarrow \gamma_{\omega_{i2}} + \gamma_{\omega_{p1}}$.

One can directly observe from figure 4-3 that the same wave component can be generated from potentially multiple different paths. As an example, we already show that an idler photon at ω_{i4} can be generated through either degenerate-pump parametric amplification, non-degenerate pump parametric amplification, or cascaded frequency conversion. This is non-coincidental because the second pump we consider here is the third harmonics of the first pump. Moreover, different idlers can interact with each

other through various two pump photon nonlinear processes. Depending on the phase matching conditions, these sideband interactions can strongly entangle a selection or all the idlers with each other. Accordingly, one cannot decouple the whole system into pairwise two-mode processes and will need to use the many-mode formalism to accurately describe the dynamics [42].

In the next section, we will develop a formal, generalized model that incorporates both the non-idealities of the pump and the many-mode dynamics.

4.5 Generalized Equations of Motions

Before deriving the generalized equations of motion for the system, let us first make a few definitions on the pump and its third harmonics. We show in section 4.2 that the pump evolution can be numerically solved using (4.2) or (4.6) to include the pump depletion effect. Without loss of generality, we can rewrite $A_{p1}(x)$ and $A_{p2}(x)$ in the rotating frame form as

$$\begin{aligned} A_{p1}(x) &= A_{p1r}(x)e^{-j\int_0^x \alpha_{p1}(x')dx'}, \\ A_{p2}(x) &= A_{p2r}(x)e^{-j\int_0^x \alpha_{p2}(x')dx'}, \end{aligned} \tag{4.7}$$

in which $A_{p1r}(x)$, $A_{p2r}(x)$ are defined to be the real, signed amplitudes of the pump and its harmonics respectively. $\alpha_{p1}(x)$, $\alpha_{p2}(x)$ encode the phase information of the pumps and bear the physical meanings of the instantaneous phase modulations at position x. We use instead the integral of $\alpha_{p1}(x)$ and $\alpha_{p2}(x)$ in the definition of the rotating frames here, as these nonlinear phase modulations terms are now spatially dependent. Notice that $A_{p1r}(x)$, $A_{p2r}(x)$ are holomorphic whereas $\alpha_{p1}(x)$, and $\alpha_{p2}(x)$ are continuous under the definition of (4.7).

To model the many-mode processes, we will use the traveling wave ansatz

$$\phi(x,t) = A_{p1}(x)e^{j(\omega_p t + k_{p1}x)} + A_{p2}(x)e^{j(\omega_{2p}t + k_{p2}x)} \tag{4.8}$$

$$+ A_s(x)e^{i(k_s x + \omega_s t)} + \sum_{m=1}^{N} A_{i,m}(x)e^{i(k_{im}x + \omega_{im}t)} + c.c., \tag{4.9}$$

in which $A_{i,m}(x)$ represent the flux amplitude of the m-th idler included in the analysis with frequency ω_{im} and wave vector k_{im}. For clarity, the main idler of the desired parametric amplification process $2\gamma_{\omega_{p1}} \rightarrow \gamma_{\omega_s} + \gamma_{\omega_{i1}}$ is chosen to have index 1. Notice that the N idlers included in the ansatz are all reachable from the signal through two-pump photon processes, so that we can still apply the generalized stiff-pump approximation and linearize the equations of motions later.

The choice of the actual number of sidebands N depends on the linear dispersion of the transmission line. As a rule of thumb, N should scale with the cut-off frequency ω_c of the transmission line. The intuition is that as the cut-off frequency increases, the group velocity dispersion (GVD) of the transmission decreases at the same frequency range, thereby making the phase mismatch conditions of processes involving higher frequency components become more favorable. Therefore one has to include more higher frequency sidebands to properly account for their contributions to the overall dynamics. We can express each frequency ω_{im} in the basis of ω_s, ω_{p1}, and ω_{p2} as

$$\omega_{im} = c_{1,m}\omega_s + c_{2,m}^{(l)}\omega_{p1} + c_{3,m}^{(l)}\omega_{p2}, \quad \text{with} \tag{4.10}$$

$$c_{1,m} \in \{-1, 1\}, \quad c_{2,m}^{(l)}, c_{3,m}^{(l)} \in [-2, 2], \quad \text{and} \tag{4.11}$$

$$\left|c_{2,m}^{(l)}\right| + \left|c_{3,m}^{(l)}\right| = 2. \tag{4.12}$$

The coefficient $c_{u,m}^{(l)}$ denotes the coefficient of the basis wave component $u \in \{1, 2, 3\}$ of idler $m \in [1, N]$ in its l-th decomposition form. the superscript (l) of the pump coefficients is necessary because an idler can have more than one decomposition forms, as the pump basis here is not minimal (basis components are not linearly independent). As an example, the main idler ω_{i1} can be decomposed as

$$\omega_{i1} = c_{1,1}\omega_s + c_{2,1}^{(1)}\omega_{p1} + c_{3,1}^{(1)}\omega_{p2} = -1 \cdot \omega_s + 2 \cdot \omega_{p1} + 0 \cdot \omega_{p2}, \quad \text{or} \tag{4.13}$$

$$\omega_{i1} = c_{1,1}\omega_s + c_{2,1}^{(2)}\omega_{p1} + c_{3,1}^{(2)}\omega_{p2} = -1 \cdot \omega_s - 1 \cdot \omega_{p1} + 1 \cdot \omega_{p2}. \tag{4.14}$$

With (4.10), the position-dependent linear and total phase mismatch of the process

$c_{1,m}\gamma_{\omega_s} + c^{(l)}_{2,m}\gamma_{\omega_{p1}} + c^{(l)}_{3,m}\gamma_{\omega_{p2}} \rightarrow c^{(l)}_{u,m}\gamma_{\omega_{im}}$ can be defined as

$$\Delta k^{(l)}_{l,(s,m)}(x) = c_{1,m}\left(k_{im} - c_{1,m}k_s - c^{(l)}_{2,m}k_{p1} - c^{(l)}_{3,m}k_{p2}\right) \tag{4.15}$$

$$= -k_s + g_{1,m}k_{im} + g^{(l)}_{2,m}k_{p1} + g^{(l)}_{3,m}k_{p2}, \quad \text{and} \tag{4.16}$$

$$\Delta k^{(l)}_{(s,m)}(x) = (k_s + \alpha_s) + g_{1,m}(k_{im} + \alpha_{im}) + g^{(l)}_{2,m}(k_{p1} + \alpha_{p1}) + g^{(l)}_{3,m}(k_{p2} + \alpha_{p2}), \tag{4.17}$$

in which we drop the explicit dependence on position x of $\alpha_s(x)$, $\alpha_{p1}(x)$, $\alpha_{p2}(x)$, and $\alpha_{im}(x)$. The coefficients $g^{(l)}_{u,m}$ are defined by (4.15) and (4.16). The overall sign coefficient $c_{1,m}$ in the expressions of $\Delta k^{(l)}_{l,(s,m)}(x)$ and $\Delta k^{(l)}_{(s,m)}(x)$ makes sure that the overall coefficient of k_s is always negative to match with the convention in [47]. Another functionality of the coefficient $c_{1,m}$ is to manifest the type of the corresponding process. Specifically, a process is parametric amplification when $c_{1,m} = -1$ and frequency conversion if $c_{1,m} = 1$. It turns out that the specific category of nonlinear process have implications on the added quantum noise [25], and the details will be discussed later in section 5.2. Moreover, (4.16) implies

$$\omega_s = g_{1,m}\omega_{im} + g^{(l)}_{2,m}\omega_{p1} + g^{(l)}_{3,m}\omega_{p2}. \tag{4.18}$$

Because the signal, the pump, and its third harmonics span all the N idlers in frequency, we can also deduce from the decompositions whether a direct interaction between an arbitrary pair of idlers is possible via a two pump photon process. From (4.10), the linear and the total phase mismatch of a potential sideband interaction

between the m-th and the m'-th idlers can be written as

$$\Delta k^{(l_m,l_{m'})}_{l,(m,m')} = c_{1,m}\left(\Delta k^{(l_{m'})}_{l,(s,m')} - \Delta k^{(l_m)}_{l,(s,m)}\right) \tag{4.19}$$

$$= c_{1,m}\left(-c_{1,m}k_{im} + c_{1,m'}k_{im'} + (c^{(l_{m'})}_{2,m'} - c^{(l_m)}_{2,m})k_{p1} + (c^{(l_{m'})}_{3,m'} - c^{(l_m)}_{3,m})k_{p2}\right)$$

$$= -k_{im} + c_{1,m}\left(c_{1,m'}k_{im'} + (c^{(l_{m'})}_{2,m'} - c^{(l_m)}_{2,m})k_{p1} + (c^{(l_{m'})}_{3,m'} - c^{(l_m)}_{3,m})k_{p2}\right) \tag{4.20}$$

$$= -k_{im} + g_{1,(m,m')}k_{im'} + g^{(l_m,l_{m'})}_{2,(m,m')}k_{p1} + g^{(l_m,l_{m'})}_{3,(m,m')}k_{p2}, \quad \textit{and} \tag{4.21}$$

$$\Delta k^{(l_m,l_{m'})}_{(m,m')}(x) = c_{1,m}\left(\Delta k^{(l_{m'})}_{(s,m')}(x) - \Delta k^{(l_m)}_{(s,m)}(x)\right) \tag{4.22}$$

$$= -(k_{im} + \alpha_{im}(x)) + g_{1,(m,m')}(k_{im'} + \alpha_{im'}(x))$$

$$+ g^{(l_m,l_{m'})}_{2,(m,m')}(k_{p1} + \alpha_{p1}(x)) + g^{(l_m,l_{m'})}_{3,(m,m')}(k_{p2} + \alpha_{p2}(x)), \tag{4.23}$$

in which the effective sideband coefficients $g_{1,(m,m')}$, $g^{(l_m,l_{m'})}_{2,(m,m')}$, and $g^{(l_m,l_{m'})}_{3,(m,m')}$ defined from (4.20) to (4.21) satisfy a similar relation

$$\omega_{im} = g_{1,(m,m')}\omega_{im'} + g^{(l_m,l_{m'})}_{2,(m,m')}\omega_{p1} + g^{(l_m,l_{m'})}_{3,(m,m')}\omega_{p2}. \tag{4.24}$$

(4.21) shows that a direct, two-pump-photon mediated interaction between the m-th and the m'-th idlers is possible if and only if

$$\left|g^{(l_m,l_{m'})}_{2,(m,m')}\right| + \left|g^{(l_m,l_{m'})}_{3,(m,m')}\right| = \left|c^{(l_{m'})}_{2,m'} - c^{(l_m)}_{2,m}\right| + \left|c^{(l_{m'})}_{3,m'} - c^{(l_m)}_{3,m}\right| = 2 \tag{4.25}$$

for some l_m and $l_{m'}$. In addition, (4.22) suggests

$$\begin{aligned} c_{1,m}\Delta k^{(l_m,l_{m'})}_{l,(m,m')} \quad + c_{1,m'}\Delta k^{(l_{m'},l_m)}_{l,(m',m)} \quad &= 0 \quad \text{and} \\ c_{1,m}\Delta k^{(l_m,l_{m'})}_{(m,m')}(x) + c_{1,m'}\Delta k^{(l_{m'},l_m)}_{(m',m)}(x) &= 0. \end{aligned} \tag{4.26}$$

Using the generalized stiff-pump approximation, we decouple the dynamics of the two pumps from the signal and its sidebands. Substituting the full ansatz (4.9) into the nonlinear wave equation (3.7) and assembling terms oscillating at the same frequencies together, we obtain a system of $N+1$ second order nonlinear differential equations for the signal and its sidebands. After we utilize the pump solution from

(4.2) or (4.6), the system of the $N+1$ nonlinear differential equations becomes linearized. To highlight the underlying physics, we transform the flux amplitudes of the signal and idlers in (4.9) into the rotating frame

$$A_s(x) = e^{j\int_0^x \alpha_s(x')dx'} A_{sr}(x), \tag{4.27}$$

$$A_{ir}(x) = e^{j\int_0^x \alpha_{im}(x')dx'} A_{ir,m}(x), \quad \text{with} \tag{4.28}$$

$$\alpha_s(x) = \frac{k_s^3(k_{p1}^2|A_{p1}(x)|^2 + k_{p2}^2|A_{p2}(x)|^2)}{8\omega_s^2}, \quad \text{and} \tag{4.29}$$

$$\alpha_{im}(x) = \frac{k_{im}^3(k_{p1}^2|A_{p1}(x)|^2 + k_{p2}^2|A_{p2}(x)|^2)}{8\omega_{im}^2}. \tag{4.30}$$

Finally, with the continuum approximation, SVEA, and the definitions in (4.7), (4.10), (4.17), and(4.23), we arrive at the many-mode equations of motion

$$\begin{aligned}\frac{\mathrm{d}}{\mathrm{d}x}A_{sr}(x) = &-j \sum_{\{n:\ c_{1,n}=-1\}} \left(\sum_{l_n} r_n^{(l_n)} \kappa_{s,n}^{(l_n)} e^{j\int_0^x \Delta k_{(s,n)}^{(l)}(x')dx'} \right) A_{ir,n}^*(x) \\ &+ j \sum_{\{m:\ c_{1,m}=1\}} \left(\sum_{l_m} r_m^{(l_m)} \kappa_{s,m}^{(l_m)} e^{j\int_0^x \Delta k_{(s,m)}^{(l)}(x')dx'} \right) A_{ir,m}(x),\end{aligned} \tag{4.31}$$

$$\begin{aligned}\frac{\mathrm{d}}{\mathrm{d}x}A_{ir,n}^*(x) = &\ j \left(\sum_{l_n} r_n^{(l_n)} \kappa_{n,s}^{(l_n)} e^{-j\int_0^x \Delta k_{(s,n)}^{(l)}(x)dx} \right) A_{sr}(x) \\ &- j \sum_{\{n':\ c_{1,n'}=-1\ \&\ n'\neq n\}} \left(\sum_{l_n} \sum_{l_{n'}} r_{(n,n')}^{(l_n,l_{n'})} \kappa_{n,n'}^{(l_n,l_{n'})} e^{-j\int_0^x \Delta k_{n,n'}^{(l_n,l_{n'})}(x')dx'} \right) A_{ir,n'}^*(x) \\ &+ j \sum_{\{m':\ c_{1,m'}=1\}} \left(\sum_{l_n} \sum_{l_{m'}} r_{(n,m')}^{(l_n,l_{m'})} \kappa_{n,m'}^{(l_n,l_{m'})} e^{-j\int_0^x \Delta k_{n,m'}^{(l_n,l_{m'})}(x')dx'} \right) A_{ir,m'}(x),\end{aligned} \tag{4.32}$$

and

$$\frac{\mathrm{d}}{\mathrm{d}x}A_{ir,m}(x) = j\left(\sum_{l_m} r_m^{(l_m)}\kappa_{m,s}^{(l_m)} e^{-j\int_0^x \Delta k_{(s,m)}^{(l)}(x)dx}\right) A_{sr}(x)$$
$$+ j \sum_{\{m':\ c_{1,m'}=1\ \&\ m'\neq m\}} \left(\sum_{l_m}\sum_{l_{m'}} r_{(m,m')}^{(l_m,l_{m'})}\kappa_{m,m'}^{(l_m,l_{m'})} e^{j\int_0^x \Delta k_{m,m'}^{(l_m,l_{m'})}(x')dx'}\right) A_{ir,m'}(x)$$
$$- j \sum_{\{n':\ c_{1,n'}=-1\}} \left(\sum_{l_m}\sum_{l_{n'}} r_{(m,n')}^{(l_m,l_{n'})}\kappa_{m,n'}^{(l_m,l_{n'})} e^{j\int_0^x \Delta k_{m,n'}^{(l_m,l_{n'})}(x')dx'}\right) A_{ir,n'}^*(x) \tag{4.33}$$

$$\text{for} \quad \{n\in[1,N]:\ c_{1,n}=-1\} \quad \text{and} \quad \{m\in[1,N]:\ c_{1,m}=1\}.$$

The additional symbols introduced in (4.31)-(4.33) are defined as follows:

$$r_m^{l_m} = (j)^{\left(c_{2,m}^{(l_m)}+c_{3,m}^{(l_m)}\right)}, \qquad r_{(m,m')}^{(l_m,l_{m'})} = (j)^{\left(g_{2,(m,m')}^{(l_m,l_{m'})}+g_{3,(m,m')}^{(l_m,l_{m'})}\right)} \tag{4.34}$$

$$\kappa_{s,m}^{(l_m)} = \frac{k_s k_{im} k_{p1}^{\left|g_{2,m}^{(l_m)}\right|} k_{p2}^{\left|g_{3,m}^{(l_m)}\right|}}{8\omega_s^2}\left(k_s + \Delta k_{l,(s,m)}^{(l_m)}(x)\right)$$
$$\cdot C_p\left((A_{p1r}(x), g_{2,m}^{(l_m)}\right)\cdot C_p\left((A_{p2r}(x), g_{3,m}^{(l_m)}\right), \tag{4.35}$$

$$\kappa_{m,s}^{(l_m)} = \frac{k_s k_{im} k_{p1}^{\left|g_{2,m}^{(l_m)}\right|} k_{p2}^{\left|g_{3,m}^{(l_m)}\right|}}{8\omega_{im}^2}\left(k_{im} - g_{1,m}^{(l_m)}\Delta k_{l,(s,m)}^{(l_m)}(x)\right)$$
$$\cdot C_p\left((A_{p1r}(x), g_{2,m}^{(l_m)}\right)\cdot C_p\left((A_{p2r}(x), g_{3,m}^{(l_m)}\right), \tag{4.36}$$

$$\kappa_{m,m'}^{(l_m,l_{m'})} = \begin{cases} \frac{k_{im}k_{im'}k_{p1}^{\left|g_{2,(m,m')}^{(l_m,l_{m'})}\right|}k_{p2}^{\left|g_{3,(m,m')}^{(l_m,l_{m'})}\right|}}{8\omega_{im}^2}\left(k_{im}+\Delta k_{l,(m,m')}^{(l_m,l_{m'})}(x)\right) & \left|g_{2,(m,m')}^{(l_m,l_{m'})}\right| + \left|g_{3,(m,m')}^{(l_m,l_{m'})}\right| = 2 \\ \cdot C_p\left((A_{p1r}(x), g_{2,m,m')}^{(l_m,l_{m'})}\right)\cdot C_p\left((A_{p2r}(x), g_{3,(m,m')}^{(l_m,l_{m'})}\right) & , \\ 0, & \left|g_{2,(m,m')}^{(l_m,l_{m'})}\right| + \left|g_{3,(m,m')}^{(l_m,l_{m'})}\right| \neq 2 \end{cases} \tag{4.37}$$

$$C_p\left(A(x), g\right) = \begin{cases} (A(x))^{|g|}, & g>0 \\ (A^*(x))^{|g|}, & g<0 \end{cases} \tag{4.38}$$

$r_m^{l_m}$ and $r_{(m,m')}^{(l_m,l_{m'})}$ are simply sign coefficients that have values of -1 or 1. Their values

are determined by the specific structure of the corresponding nonlinear process. $\kappa_{m,s}^{(l_m)}$ and $\kappa_{s,m}^{(l_m)}$ are the coupling coefficients that couple a signal photon to a m-th idler photon through the process $c_{1,m}\gamma_{\omega_s} + c_{2,m}^{(l_m)}\gamma_{\omega_{p1}} + c_{3,m}^{(l_m)}\gamma_{\omega_{p2}} \rightarrow \gamma_{\omega_{im}}$ and vice versa. $\kappa_{m,m'}^{(l_m,l_{m'})}$ is the coupling coefficient that couples a m'-th idler to a m-th idler through the process $g_{1,(m,m')}\gamma_{\omega_{im'}} + g_{2,(m,m')}^{(l_m,l_{m'})}\gamma_{\omega_{k_{p1}}} + g_{3,(m,m')}^{(l_m,l_{m'})}\gamma_{\omega_{k_{p2}}} \rightarrow \gamma_{\omega_{im}}$. It is non-zero only when the condition of (4.25) is satisfied, which simply means that there has to exist such a direct two-pump-photon process to couple these two idlers.

The right hand side of (4.31) divides the N idlers into two categories: each idler n in the first set $S_1 = \{n \in [1, N] : \ c_{1,n} = -1\}$ interacts with the signal through a parametric amplification process, whereas each idler m in the second set $S_2 = \{m \in [1, N] : \ c_{1,m} = 1\}$ interacts with the signal through a frequency conversion process. Similarly, the division of idlers done on the right hand sides of (4.32) and (4.33) shows that the two set of idlers S_1 and S_2 are both invariant with respect to frequency conversion transformations. An idler n in S_1 can interact with an idler m in S_2 only through a parametric amplification process, provided that such a two-pump photon process exists.

The generalized multi-mode equations of motion (4.31)-(4.33) are the main result of this section. This general model allows for an arbitrary number of signal sidebands to be included. The generalized model will exactly reduce to the standard two-mode model in (3.22) if we set $N = 1$, use the same constant pump condition, and let the only sideband to be the main idler of the desired signal parametric amplification process. Even though we utilized the continuum limit approximation in deriving the final results, our generalized model will still approximate the dynamics well even when relatively high frequency sidebands are included. This can be understood from the same argument in section 5.2 that the continuum limit approximation can be alternatively understood as a perturbative expansion around the corresponding linear transmission line. Consequently, the continuum limit approximation should still be valid as long as the nonlinear interactions at high frequency sidebands are sufficiently weak due to either a weak nonlinearity or a huge phase mismatch.

The generalized model presented here includes the effect from both the original

pump and its third harmonics. This is because the THG captures the overall pump dynamics quite well in the specific device [38] we are analyzing. However, the model can be easily extended to adopt arbitrary pump conditions by adding additional wave components into the pump basis, as long as overall the pump components altogether solve the original nonlinear wave equation (3.7). As an example, if the sixth harmonics of the pump turns out to be non-negligible for another device design, one will use instead the decomposition

$$\omega_{im} = c_{1,m}\omega_s + c^{(l)}_{2,m}\omega_{p1} + c^{(l)}_{3,m}\omega_{p2} + c^{(l)}_{4,m}\omega_{p3} \tag{4.39}$$

to replace (4.10), with ω_{p3} representing the sixth harmonics. In addition, the generalized model considers only the lowest fourth-order nonlinearity. This is valid as long as the sixth-order nonlinearity term, the next lowest order in the expansion, is sufficiently smaller. Indeed, using typical circuit parameters and an initial pump current $I_{pn} = 0.78 \cdot 0.91 = 0.71$, we see that

$$\left|\frac{E_J\phi_x^4\phi_{xx}/4!}{-E_J\phi_x^2\phi_{xx}/2!}\right| = \left|\frac{\phi_x^2}{12}\right| \sim \left|\frac{k_p^2 A_p^2(0)}{12}\right| \sim 0.04 \ll 1, \tag{4.40}$$

which means the contributions from the next lowest order nonlinearity is negligible and justifies the use of the lowest order nonlinearity only. In the next section, we will calculate the gain dynamics of the system calculated by the generalized multi-mode model and compare the results with that calculated by the standard two-mode model.

4.6 Signal Dynamics with Many-Mode Interactions

We will now systematically make changes to the model and evaluate the outcome at each step to better understand the effects of each of the non-idealities. We will use a 5.983 GHz signal as used in [38] for illustration, but tune the pump frequency slightly near the resonance feature to optimally phase match the desired parametric amplification process. A similar tuning procedure is performed during the experimental characterization of JTWPAs. In the remainder of the this section, we will consider

the pump attenuation effect by using the pump condition shown in figure 4-2, but still assume the signal and all the sidebands to be lossless in order to separate the effects of the multiple modes from the quantum efficiency degredation due to attenuation. Although the distributed attenuation introduces additional quantum noise and reduces the quantum efficiency, the total attenuation is on the order of 2 dB in a ~ 2000 unit cell device and has a minimal effect on the dynamics (other than scaling down the overall gain).

We start by evaluating the effect of the pump current normalization on the signal dynamics with only one sideband (main idler). Figure 4-4 plots the normalized power gain of the signal and idler with the raw (dashed) and re-normalized (solid) initial pump current condition as a function of position x. Without the new normalization in the initial pump current, the computed gain at the end of the device is on the order of 60dB, an unrealistic value that is far from the experimentally measured values. With the new initial pump current normalization, the signal gain at the end of the device comes down to $\sim$ 35dB, which is much closer to the measured lossless values ($\sim$ 25dB) but still an order of magnitude higher. For the remainder of this section, we will assume the use of the re-normalized initial pump current value $I_{pn} = 0.71 I_0$ unless specified otherwise.

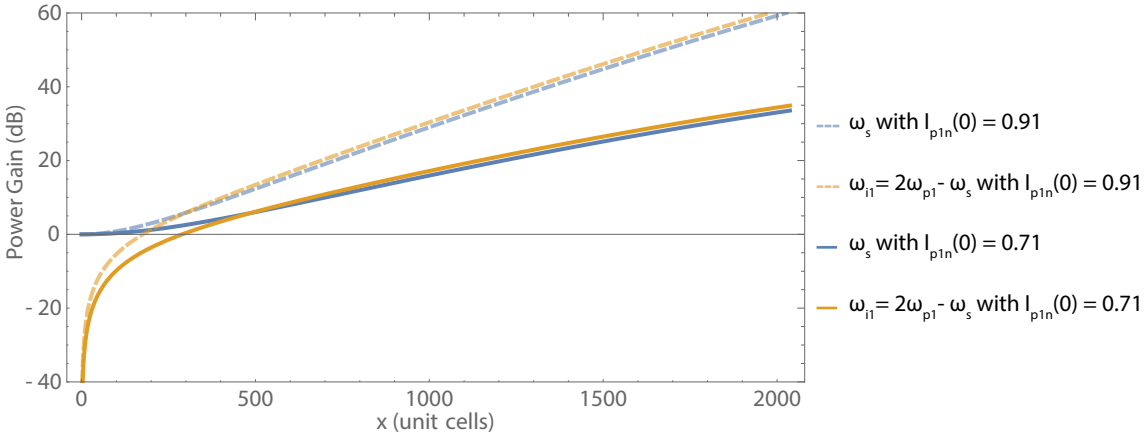

Figure 4-4: Normalized power gain of the signal and idler as a function of position x. Dashed lines represent the gain dynamics with an initial input pump current of $I_p(0) = 0.91 I_0$, whereas the solid lines represent the gain dynamic with the re-normalized initial input pump current of $I_p(0) = 0.78 \cdot 0.91 I_0 = 0.71 I_0$.

Next, we valuate the effect of the third harmonics on the signal dynamics still with only one sideband (main idler). Figure 4-5 plots the normalized power gain of the signal and idler with two different pump conditions. The solid lines represent the gain dynamics under the influence of the THG pump modulation, whereas the dashed lines represent those under the original pump only. We observe that the calculated gain values of the signal and idler under the two different pump conditions start off very similarly and then diverges from each other with different slopes (in the dB scale). Near the end of the device the calculated gain under different pump conditions differ by each other by $\sim$ 12dB when the signal gain in the single pump case is at the level of 20dB. This drastic difference in the calculated gain level is due to two major effects. First, the average pump power decreases because of the THG, and therefore the effective coupling strength of the parametric amplification is smaller than the THG-free case. Second, the effective phase mismatch of the parametric amplification under different pump conditions are different. The THG modulation of the pump results in an additional phase mismatch term whose magnitude is proportional to the periodicity of the elliptical function in the analytical solution of the third harmonic generation. Because the phase mismatch in the single pump case is fitted to be close to zero, the parametric amplification process with pump THG becomes poorly phase mismatch. Moreover, we see a modulation in the relative magnitudes of the signal and idler gain, which is also an effect of the pump modulation. Figure 4-5 confirms that the effect from the THG of the pump is non-negligible and affects the choice of both design parameters and operating points.

We now evaluate the effect of additional sidebands on the signal gain dynamics using only the original pump. The sidebands are sorted by frequency in increasing order. For instance, $\omega_{i2} = 2\omega_{p1} + \omega_s$, $\omega_{i3} = 4\omega_{p1} - \omega_s$, $\omega_{i4} = 4\omega_{p1} + \omega_s$, and so forth. Figure 4-6(a) plots the signal gain as a function of position x with various number of sidebands N included. We clearly see that the introduction of additional sidebands drastically change the signal evolution, and the signal behaviors starts to converge from $N = 5$. The reason for the signal gain to decrease with the number of sidebands included is that the additional sidebands not only consume power from the signal

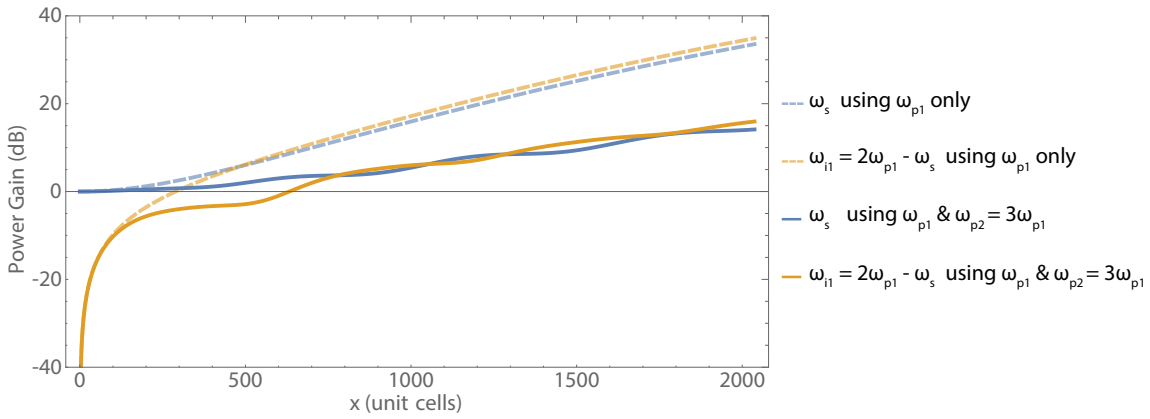

Figure 4-5: Normalized power gain of the signal and idler as a function of position x. Dashed lines represent the gain dynamics with the effect of the original pump only, whereas the solid lines represent the gain dynamic with the effects of THG.

and idlers but also introduce effective modulations and therefore additional phase mismatch to the main parametric amplification process of the signal. Notice that here we did not consider the THG dynamics, and again the original phase mismatch of the simplified two-mode parametric amplification process is fitted to be very close to zero. Consequently, One should not be surprised that the gain of the signal at $N = 7$ in figure 4-6(b) drops to a level even significantly below the experimentally measured value at this stage.

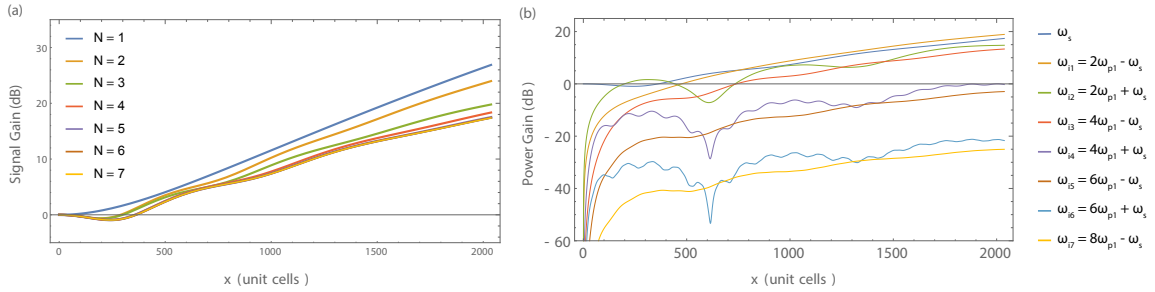

Figure 4-6: (a) Signal power gain as a function of position x with varying number of sidebands N included in the model. (b) Gain dynamics of the signal and the sidebands at $N = 7$.

Finally, we put everything together by applying the generalized model (4.31)-(4.33) at $N = 7$ with the THG pump condition. Figure 4-7 shows the full gain

dynamics and the gain spectrum computed by our generalized model. The signal gain at the end of the device is computed to be 22.8dB, which is comparable to the experimentally measured value ($\sim$ 25dB). As a comparison, the standard model using a re-normalized pump initial condition predicts $\sim$ 35dB gain at the end of the device. It is important to note that the particular computed gain value of our generalized model presented here was not fitted or optimized: all we have done to get this value are simply taking the experimentally extracted circuit parameters of [38] and using instead the re-normalized initial pump condition for numerical calculation. This suggests that our generalized model is able to reproduce the experiment results fairly closely, and this agreement is neither a coincidence nor an overfit. Another important observation from figure 4-7 is that the idlers $\omega_{i2} = 2\omega_{p1} + \omega_s$ and $\omega_{i3} = 4\omega_{p1} - \omega_s$ that are next lowest in frequencies are strongly coupled to the principal signal and idlers, which not only divert power from the signal but also introduces additional fluctuations [42]. In fact, we will show in section 5.2 next that these strongly interacting sidebands are the most responsible for the added noise and reduction in quantum efficiency of the JTWPA.

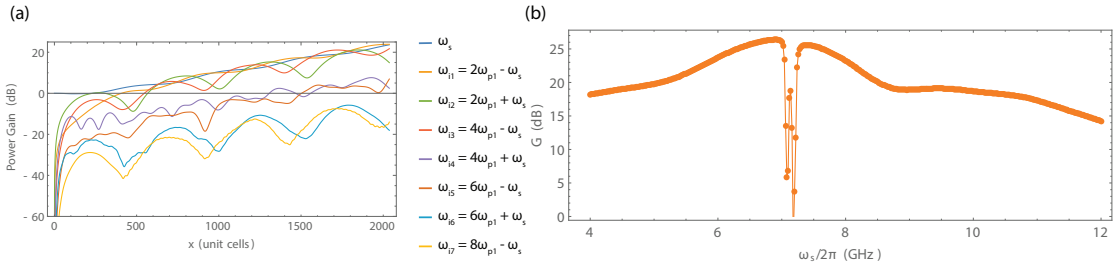

Figure 4-7: (a) Gain dynamics of the signal and its sidebands as a function of position x and (b) signal gain as a function of signal frequency computed by the generalized multi-mode equations of motions (4.31)-(4.33) at $N = 7$.

One might note that the computed signal gain by the generalized model, albeit neglecting signal attenuation, is still lower than the measured value. Other factors such as imperfect impedance matching between the JTWPA and the 50Ω cables should further decrease the measured gain, which ultimately should always be several dBs lower than the theoretical prediction. This means that our computed gain is

still about $6-7$dB lower than the true theoretical value. One explanation to the underestimation of signal gain is that the initial pump current we used is only a crude estimate and has not been formally optimized. While this explanation is plausible, it turns out that there is another subtle cause to the underestimation in gain: the SVEA. In the next section, we will further discuss the ramifications of applying SVEA in JTPWA analyses.

4.7 Beyond the Slowly Varying Envelope Approximation

The SVEA has been widely used in the field of nonlinear optics and is often valid in most of the applications. Only in very rare cases such as the modeling of the self-focusing, sub- or few-optical-cycle ultra-short pulses do SVEA start to break down [55, 54, 36]. The commonly used form of SVEA presented in section 3.3 can be understood in time domain as the condition that the envelope of a traveling wave pulse varies very slowly during one optical cycle. The corresponding frequency-domain interpretation is that the spectral linewidth of the traveling wave is much narrower than the center/carrier frequency. For this reason, SVEA is therefore also sometimes referred as the "narrow-band approximation". Alternatively, SVEA dictates that the field varies slowly and cannot be reasonably amplified within a wavelength, and the interaction time is much larger than an optical cycle [7]. These conditions are in general well satisfied in optical parametric amplifiers (OPAs) operating at telecommunication wavelengths because the typical fiber nonlinearity is sufficiently small.

For Josephson junction based microwave nonlinear devices, the junction nonlinearity is orders of magnitude larger than that of a typical nonlinear optical fiber and can therefore result in ultra-strong nonlinear couplings. As a comparison, the nonlinear coefficient of a typical high nonlinearity fiber (HNLF) is $\gamma_{\mathrm{HNLF}} = g_{\mathrm{HNLF}}\mathrm{P}^{-1} = 11.4\ \mathrm{W}^{-1}\cdot\mathrm{km}^{-1} \approx 1.767\cdot 10^{-9}\mathrm{W}^{-1}\lambda_0^{-1}$ for $\lambda_0 = 1550$nm [63]. The resulting gain per wavelength of the HNLF is then $g_{\mathrm{HNLF}} = 3.53\cdot 10^{-6}\lambda_0^{-1}$ when operating at a high

pump power of P = 2kW. For the RPM JTWPA considered in [38], a 6GHz signal is amplified by > 20dB in 2000 unit cells at a pump power of -67dBm. Hence, its nonlinear coefficient and gain per wavelength can be estimated to be $\gamma_{\mathrm{JJ}} \sim 6.75 \cdot 10^8\ W^{-1}\lambda_0^{-1}$ and $g_{\mathrm{JJ}} \sim 0.135\lambda_0^{-1}$ respectively. We see that the nonlinearity of a Josephson Junction is in excess of four orders of magnitude larger than that of the HNLF. Moreover, the signal is "sensibly" amplified by ~ 1.05 times in 92 unit cells or one wavelength. These facts altogether imply that the SVEA becomes marginally valid in JTWPA analyses and therefore motivate us to carefully evaluate its effect on the system dynamics. One straightforward way to validate SVEA is to solve the full nonlinear wave equation without approximation and compare the numerical results to those with SVEA applied.

To isolate out the sole effect of SVEA on the parametric amplification, let us take a few steps back and start by investigating on the simplest problem as possible: a perfect-two mode parametric amplification process mediate by a constant pump (without attenuation). Figure 4-7 plots the parametric power gain of the signal and idler solved using different degrees of approximations. When the parametric gain predicted by the analytical formula (with SVEA applied everywhere, case (1)) is at 20dB, we observe a 1.2dB increase in signal gain when we lift the SVEA on the signal and idler (while still applying SVEA to the pump, case (2)). The signal gain is then further increased by another ~ 3.5dB after we relax the SVEA on the pump as well (case (3)). This reveals that applying SVEA on either the signal or the pump will lead to an underestimation in the signal gain.

Furthermore, figure 4-7 also provides insights into the differences in the effect of SVEA when applied to different wave components. Specifically, the amount of underestimation resulted from applying the SVEA to the pump is noticeably larger than that resulted from instead applying the SVEA to the signal and idler. By comparing the gain dynamics in case (1) and (2) (both use SVEA on the pump), we see that the signal gain values calculated with and without SVEA on the signal and idler closely follow each other at first and then only start to appreciably deviate from each other after the signal has been significantly amplified. In other words,

the effect of SVEA on the signal and idler only becomes significant at high signal gain levels near the end of the device. In contrast, the signal gain values computed with and without SVEA on the pump in case (2) and (3) respectively (neither uses SVEA on the signal and idler) are notably different from the very beginning, and the asymptotic slope of the signal gain without using SVEA on the pump in case (3) is noticeably larger than that in case (2) when the SVEA on the pump is instead used. This is because the pump power is at a significantly high level from the start, and the non-negligible higher order derivatives of the pump act effectively as additional polarization sources driving the desired parametric amplification process throughout the device. This explains why the effect of SVEA on the pump is more significant than the effect of SVEA on the signal and idler, although the latter is also non-trivial in the JTWPA.

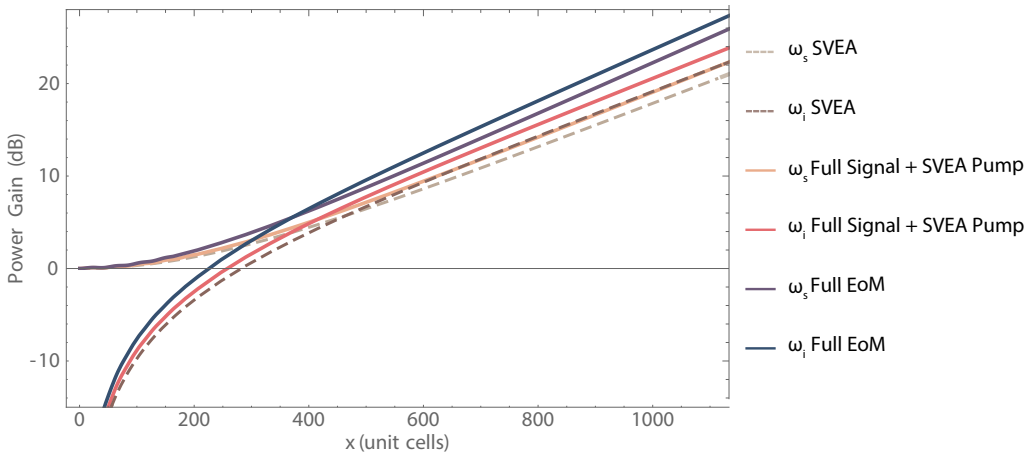

Figure 4-8: Parametric gain of the signal and idler normalized to initial signal power computed using different degrees of SVEA in an ideal two-mode parametric amplification process with a constant pump current $I_p = 0.71I_0$. Dashed lines represent the analytical signal and idler gain when the SVEA is applied to all the wave components. The nude and light pink solid lines represent the signal and idler gain when SVEA is lifted for the signal and idler but still applied to the pump. The purple and dark blue solid lines represent the signal and idler gain when SVEA is not used at all.

Finally, we relax the SVEA on the multi-mode equations of motion completely and numerically compute the system dynamics. Figure TODO plots the power gain of the JTWPA as a function of position x in (a) and as a function of signal frequency

in (b) using otherwise the same setup as in figure 4-7 except without applying SVEA. The computed signal gain at the end of the device is 42dB, which is significantly higher than the SVEA value.

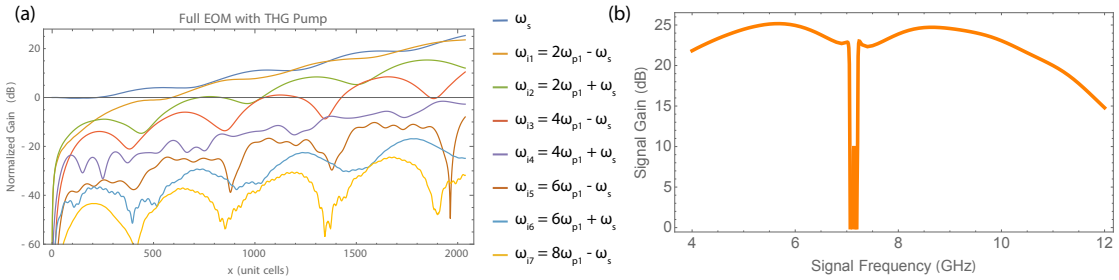

Figure 4-9: Multi-mode dynamics of the system without using SVEA. the parameters used here are exactly the same as those used in figure 4-7. (a) Non-SVEA gain dynamics of the signal and its sidebands as a function of position x. (b) Non-SVEA signal gain as a function of signal frequency computed by the generalized multi-mode equations of motions (4.31)-(4.33) at $N = 7$.

4.8 Summary

In this chapter, we revisited and evaluated each of major approximations and assumptions made in deriving the standard two-mode model of the JTWPA in section 3.3. We found out that the THG dynamics of the pump significantly affects the signal gain through a reduction in the average coupling strength and the introduction of an additional phase mismatch from modulation. Furthermore, we showed that initial pump current needs to be adjusted accordingly to make sure the total current of the pump and its third harmonics does not exceed the critical current. We then presented the generalized multi-mode model to account for the effects of the sidebands and confirmed through numerical calculation that the inclusion of sidebands does alter the system dynamics significantly. Combined with all the aforementioned corrections, our generalized multi-model is able to predict a much more realistic signal gain. Finally, we showed that applying SVEA on either the signal or the pump would result in an underestimation of the parametric gain of the JTWPAs, as the junction nonlinearity

is strong enough to make the SVEA become only marginally stable.

The standard two-mode model (3.22), albeit simple and instructive, hides away many of the non-idealities of a JTWPA. The generalized multi-mode model we developed in this chapter lies the ground work for the quantum efficiency analysis. It allows for the inclusion of arbitrary number of sidebands and captures the effect of sideband interactions to the many-mode dynamics. In the next chapter, we will apply our generalized model to deduce the JTWPA quantum efficiency.

Chapter 5

Quantum Efficiency of JTWPAs

This chapter is divided into three major parts. In the first part, we will briefly review several figures of merits relevant to the noise performance and efficiency of linear, phase-preserving (or phase-insensitive) amplifiers. In the second part, we will utilized the generalized multi-mode formalism developed in the last chapter to analyze the quantum efficiency of a typical JTWPA [38]. We aim at unraveling the cause of the unaccounted reduction in the quantum efficiency and identifying the main limiting factors. In the third part, we will contrive potential fixes to the issues identified from the first part and propose a realistic new design of a JTWPA with much improved quantum efficiency.

5.1 Introduction

The signal-to-noise ratio (SNR), the definition of which is self-explanatory from the name, is one of the most commonly used figure of merit for both classical and quantum amplifiers. It characterizes how well the signal level and the noise floor are separated from each other. For a linear amplifier operating in the single photon regime ($\langle\hat{n}\rangle = \langle\hat{a}^\dagger\hat{a}\rangle \sim 1$), the SNR can be written as

$$\mathrm{SNR} = \frac{\langle\hat{n}\rangle^2}{\langle\delta\hat{n}^2\rangle}, \tag{5.1}$$

in which $\langle \delta \hat{n}^2 \rangle = \langle \hat{n}^2 \rangle - \langle \hat{n}^2 \rangle$ is the photon number uncertainty. The noise figure F is defined as the ratio of the input SNR to the output SNR in decibel scale, although this terminology is frequently used interchangeably to the linear-scale definition noise factor. For consistency, We will use the same vocabulary as those used in [25, 42] and refer to the noise figure F as the linear SNR ratio. More specifically,

$$F = \frac{\mathrm{SNR}_i}{\mathrm{SNR}_o}, \tag{5.2}$$

in which the subscripts i and o denotes the amplifier input and output respectively. We will use NF to denote the noise figure in the decibel scale instead. The quantum efficiency has several alternative definitions. For a classical amplifier, the quantum efficiency is commonly defined as the ratio of the input noise to the output noise. In the quantum regime, the quantum efficiency is defined similarly as [12]

$$\eta = \frac{1/2}{1/2 + A}, \tag{5.3}$$

in which A is the Cave's added photon number. We see that the classical quantum efficiency can be reduced to the quantum version when the input noise approaches the fundamental limit of 1 / 2 of a photon in the limit of zero temperature [26, 25, 12]. It worth pointing out that an alternative definition $\bar{\eta} = 2\eta$ of quantum efficiency [9] is also commonly used for parametric amplifiers in literature. This is motivated by the fact the quantum efficiency of a perfect two-mode parametric amplifier approaches 50% using the definition of η at high gain. The alternative definition $\bar{\eta}$ therefore signifies the relative performance of an parametric amplifier to the theoretical limit. In fact, the definition of $\bar{\eta}$ can also be interpreted as the fraction of the total information that is collected. In this interpretation, $\bar{\eta}$ emphasizes that no information is really lost but rather "beam-split" into the other mode of a perfect two-mode parametric amplifier [39]. The aforementioned quantum efficiencies values of the JTWPAs are defined in $\bar{\eta}$. To avoid confusion, we will also use $\bar{\eta}$ and refer to it as the adjusted quantum efficiency in our analysis to allow for direction comparisons.

5.2 Quantum Efficiency of the RPM JTWPAs

In this section we will analyze the quantum efficiency of the JTWPAs using the theoretical framework developed in [42]. As already mentioned in Chapter 3, the quantum version of the equations of motion for a multi-mode system are the same as those derived using the classical Lagrangian formulation with the classical amplitudes substituted by the quantum field operators. The quantum effects arise from the non-commuting relations of the field operators [42]. We now promote our generalized equations of motion equations (4.31) to (4.33) into the quantum version using the substitution rules

$$\phi(x) \to \hat{\phi}(x), \quad A_m(x) \to d_m \hat{a}_m(x), \quad \text{and} \quad A_n^*(x) \to d_n \hat{a}_n^\dagger(x), \tag{5.4}$$

in which $d_m = \sqrt{\frac{n(\omega)\omega_c^2}{16\pi\omega\omega_J}}$ (see (3.16)) are the constant normalization factors such that the number operator $\hat{a}_m^\dagger(x)\hat{a}_m(x)$ is normalized in the unit of photon flux. By now the physical significance of sidebands in different categories should become self-evident: sidebands coupled with the signal through parametric amplification processes introduce additional quantum contributions to the variance of the signal output because their operators ($\hat{a}_m^\dagger$) do not commute with the signal operator $\hat{a}_s$.

Because we only considered two-pump-photon processes and treated the pumps classically (stiff-pump approximation), The governing system of equations is a linear, "time" (position) variant first-order autonomous system whose solution is uniquely determined by the initial condition. Notice that this is still true for the full equations of motion without using SVEA, even though they are second-order differential equations. We can therefore write its solution in the standard transfer function form

$$[\hat{a}_s(x), \hat{a}_m^{(\dagger)}(x), ...]^T = B(x) = M(x, x_0)A(x_0), \tag{5.5}$$

in which the $(N+1) \times 1$ column vector $B(x)$ describes the field operators at position x, and $M(x, x_0)$ is the $(N+1) \times (N+1)$ position-variant transfer matrix that relates the fields at position x and x_0 and satisfies $M(x, x) = I_{(N+1)}$.

One convenient way to solve the transfer matrix $M_(x, x_0)$ of creation and annihilation operators at x is to instead solve for the transfer matrix $\tilde{M}(x, x_0)$ in the flux operator basis

$$\Phi(x) = \begin{bmatrix} \hat{\phi}_s(x) \\ ... \\ \hat{\phi}_N^{(*)}(x)] \end{bmatrix} = \begin{bmatrix} d_0 & & \\ & \ddots & \\ & & d_N \end{bmatrix} B(x) = S \cdot B(x), \tag{5.6}$$

in which the (N+1)×1 vector $\Phi(x)$ describes the flux operators of signal and sidebands, and S described the constant transformation matrix that transforms the creation and annihilation operators to the flux operators. For each position x (device length), we numerically solve the differential system with respect to the flux operators $N + 1$ times, each time using an initial vector that is linearly independent with the rest of the initial conditions. This allows us to extract $\tilde{M}(x, x_0)$ that satisfies the relation

$$\Phi(x) = \tilde{M}(x, x_0)\Phi(x_0). \tag{5.7}$$

Finally, because S is a diagonal matrix and therefore invertible, we get the desired transfer matrix by applying the similarity transformation

$$M(x, x_0) = S^{-1}\tilde{M}(x, x_0)S. \tag{5.8}$$

Following the procedures outlined in section 7 of [42], we can write the signal noise figure F of the multi-mode systems in the limit of $\langle \hat{n}_{a,s} \rangle^2 \gg 1$ as

$$F_i \approx 1 + \sum_{k \neq i} |\mu_{ik}|^2 / |\mu_{ii}|^2 = \sum_k |\mu_{ik}|^2 / |\mu_{ii}|^2 , \tag{5.9}$$

in which μ_{mn} denotes the matrix element of $M(x, x_0)$ on the m-th row and n-th column, i is the index of signal in the field vectors (1 in our case).

To correctly predict the quantum efficiency of the JTWPA at 20 dB level of gain, we tune the pump frequency near the phase-matching resonance slightly to recover the same level gain for both the constant and modulated pump conditions. Figure 5-1

plots the signal gain, noise figure, and adjusted quantum efficiency at $\omega_s/(2\pi) - 5.9833$ GHz. different initial pump currents. The pump is biased at $\omega_{p1} = 7.135$GHz. With an insertion loss of ~ 1.6dB, the effective signal gain translates to about $21.6 + 1.6 \approx$ 23dB in our lossless model (for the signal and idlers). This corresponds to a initial pump current around $I_p = 0.64 I_0$ as indicated by the gray dashed line. We see that indeed the quantum efficiency predicted by using a constant (orange) and THG modulated pump (blue) are different from each other even at the same gain level. At $I_p = 0.64 I_0$, the quantum efficiency is predicted to be around 82% and 72% when using a constant and a THG modulated pump condition respectively. The quantum efficiency of the device when the third harmonics of the pump is present is lower than that when the third harmonics is not agrees with our discussion in chapter 4. Our model using either of the pump condition matches relatively well with the experimentally extracted intrinsic quantum efficiency value $85\% \pm 10\%$, with the uncertainty attributed to possible systematic errors in characterization [38]. We see that the quantum efficiency can drift either higher or lower as we vary the pump current around.

Another interesting observation on figure 5-1 (a) is that the signal gain calculated with the THG modulated pump condition does not increase monotonically with increasing pump current. Rather, the predicted gain in the THG modulated pump case oscillates around an equilibrium slope, in this case very close to that in the constant pump case. This resembles the experimentally observed behavior in figure 3-4 (a), in which the signal gain slumps with increasing pump current near $I_p = 0.8 I_0$ (without using our modification). To make things more interesting, the quantum efficiency at the slightly lower signal gain near $I_p = 0.91 I_0$ is actually higher than that at the gain peak. This behavior is also observed in our model, in which the quantum efficiency predicted using the THG modulated pump condition monotonically increases at pump current larger than 0.64 while the signal oscillates. This suggests that the third harmonics might be a possible cause to such observed behaviors.

In Figure 5-2 we plot the adjusted quantum efficiency and the noise figure as a function of position in panel (a) and (b) respectively at signal frequency 5.9833 GHz.

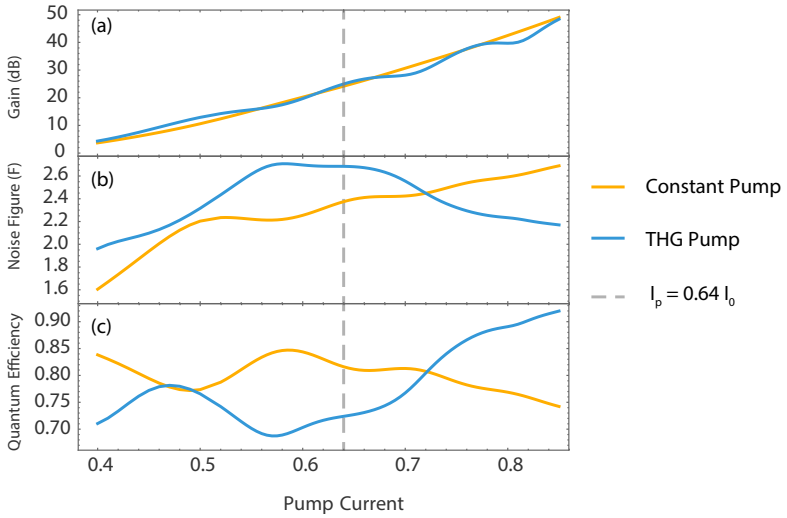

Figure 5-1: The (a) signal gain, (b) noise figure, and (c) adjusted quantum efficiency of the RPM JTWPA as a function of pump current. The pump is biased at 7.135 GHz to recover similar level of gain for the two different pump conditions. Dashed line denotes the pump current $I_p = 0.64I_0$ at which the signal gain is close to 23 dB (experimental value without insertion loss). SVEA was not used in generating the figures here.

The pump current and the pump frequency used in (a) and (b) are the same as that indicated by the gray dashed inline in figure 5-1 ($\omega_{p1} = 7.135$ GHz, $I_p = 0.64I_n$).In panel (b) we plot the noise figure (light purple) and the quantum efficiency (cyan) predicted by the THG modulated pump condition as a function of signal frequency. We see that the range of the quantum efficiency spans from as low as 50% (immediate outside the resonance linewidth) to as high as $> 95\%$ in the spectral range of interest. The result here is again in reasonable agreement with the experiments. In fact that the quantum efficiency can vary

For completeness, we discuss here the other factors that could contribute the additional quantum noise but was not accounted for. As already hinted on earlier, our model assumes the signal and all the interacting sidebands to be lossless, although we did incorporate the dielectric loss for the pump and its third harmonics to more accurately model the system dynamics. The reason is that the formalism [42] we use to calculate the quantum noise and subsequently the quantum efficiency are only valid when the system of equations are linear and conserves energy. Therefore the

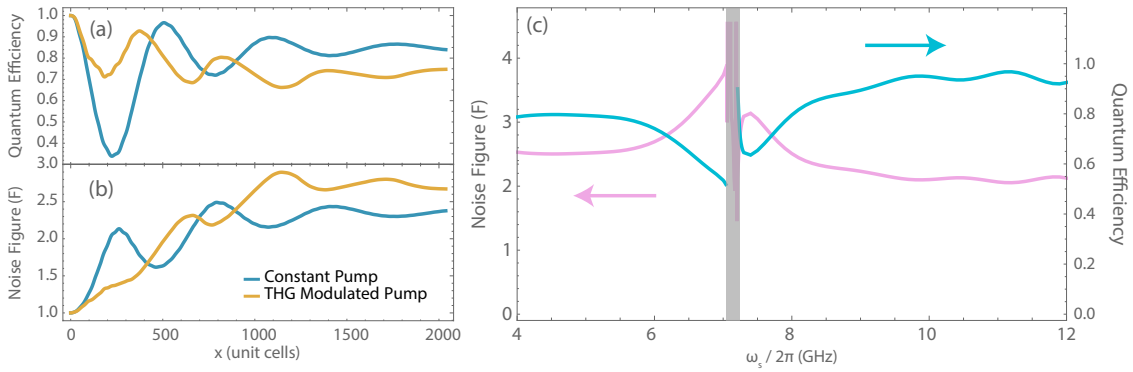

Figure 5-2: (a) The adjusted quantum efficiency and (b)the signal noise figure in the constant pump (blue) and the THG modulated pump (orange) case as a function of position x at signal frequency $\omega_s/(2\pi) = 5.9833$ GHz. (c) The noise figure (light purple) and the adjusted signal quantum efficiency (cyan) as a function of signal frequency. The pump frequency is 7.135 GHz with initial current $I_p = 0.64I_0$ for all three subfigures. The shaded area represent the narrow linewidth of the dispersion feature introduced by the phase matching resonators. The quantum efficiency was not plotted in the shaded region because the signal has very small to no gain in the immediate vicinity of the resonance and that the adjusted quantum efficiency is only well defined in high gain regime. SVEA was not used in solving the multi-mode equations of motion.

non-trivial insertion loss for the signal and idlers ($\sim 1.6dB$) will introduce additional quantum noise according to the dissipation-fluctuation theorem. [13] and [29] have used the beam splitter model to incorporate propagation losses for a two-mode system, but a model applicable to multi-model dynamics has still not been developed. Another motivation for not treating loss in the most stringent way possible is that it would not yield any new insights even when a more accurate results is obtained, as the relation between dissipation and fluctuation is long understood. We are instead more interested in the other non-ideal dynamics that could be potentially ameliorated or even eliminated once when they are understood.

Moreover, we did not account for nonlinear processes that are nonlinear with respect to the signal or the sidebands, although being a very good approximation. Furthermore, as can be indicated in the computed quantum efficiency results, treating the pump dynamics using a single THG process is likely in sufficient. In fact, the third harmonic population likely have been overestimated and consequently resulting

in a slightly underestimated quantum efficiency. For instance, all the high harmonics can in fact form snoidal waves [48] that the mere pair of the pump and its third harmonics do no approximate well on their own. However, the treatment of including in the effect of third harmonics is still valuable for understanding the system dynamics. In many cases the prediction from using a THG modulated pump condition can give reasonable estimates on the lower bound of the quantum efficiency. The information that an excess population of the third harmonics can not only decrease dynamic range but also degrade quantum efficiency is already valuable to future quantum-limited amplifier designs on its own.

Finally, when the typical pump power used to operate the JTWPA is high enough, the effects of next higher order nonlinearity (sixth) also start to to grow and becomes non-trival (see Chapter 4). In summary, our generalized multi-mode model is able to explain and estimate the experimentally extract quantum efficiency to a fairly good extent, despite not incorporating every possible non-idealities. We have also identified the major cause to the quantum efficiency reduction in JTWPA to be the lowest frequency signal and idlers sidebands. Lastly, we showed that SVEA is in some cases not strictly accurate in JTWPA anlaysis because of the incredible strong nonlinearity of the Josephson junctions. We believe the multi-mode theory developed in this thesis could serve as a valuable tool for designing future generations JTWPAs.

5.3 Design of a High Quantum Efficiency JTWPA

In the last section, we have identified the limiting factors of the device quantum efficiency to be the first few lowest frequency sidebands in frequency using the generalized multi-mode model. With this knowledge in mind, we will discuss dispersion techniques to ameliorate those issues and propose a new JTWPA design with a potentially much improved quantum efficiency. Finally, we will apply our generalized multi-mode model to validate and predict the performance of the new design and discuss the impacts of our dispersion techniques to the other figure of merits dynamic range and bandwidth.

5.3.1 Dispersion Engineering

We see from figure 4-9 that the idlers $\omega_{i2} = 2\omega_{p1} + \omega_s$ and $\omega_{i3} = 4\omega_{p1} - \omega_s$ diverts a significant amount of power from the signal and idler of the principle parametric amplification process. To suppress the coupling of these sidebands to the signal in a broadband fashion, we can engineer the dispersion of the transmission line to exacerbate the phase mismatch of the corresponding nonlinear processes. Recall that the effective phase mismatch of any fourth-order nonlinear process can be divided into the linear and nonlinear contributions $\Delta k = \Delta k_l + \Delta k_{nl}$. Because transmission lines are commonly designed to have normal dispersion (i.e. with a positive GVD), the linear phase mismatch Δk_l for all the cascaded frequency conversion and degenerate-pump parametric amplification processes in consideration are always negative in our choice of convention (see section 3.4). Furthermore, Δk_{nl} of these processes are also usually negative at normal pump power levels due to the particular sign of the junction nonlinearity. These conditions altogether necessitate the use of additional dispersion features to phase match the principal non-degenerated parametric amplification process, as previously illustrated in Figure 3-2. In the RPM technique, the desired parametric amplification is phase matched by the weak resonance feature introduced near the pump. Because the phase velocities at frequencies farther away from the pump are minimally affected by the weak resonance, we have the freedom of separately engineering the dispersion of higher frequency idlers without significantly affecting the phase matching condition of the desired amplification process.

We propose to suppress the aforementioned undesirable sideband processes by reducing the cut-off frequency of the transmission line. Depending on the specific target value, one can do so by simply adjusting the circuit design parameters (i.e., reducing the junction critical current or increasing the ground capacitance) or by using junction arrays for a even more drastic reduction [41]. As the cutoff-frequency decreases, the linear phase mismatch at the same frequency range will increase due to a larger GVD. We claim that its effect on the higher frequency sidebands are more acute than those on the lowest frequency signal and idler. Consider the same circuit

design in figure 3-1 but without the weakly coupled phase matching resonators for now, the wave vector of the transmission line with a discrete unit cell size can be solved using ABCD matrix [51] and have the analytical form of [71]

$$k_a(\omega) = 2\arcsin\left(\frac{\omega}{2\sqrt{1-\beta\omega^2}}\right). \tag{5.10}$$

Recall that equation (5.10) is written in the normalized units, so that the dependence of the wave vector on the cut-off frequency ω_c is implicitly embedded in the normalized frequency terms ω. It turns out that the true cut-off frequency ω_t of this finite unit cell size transmission line is

$$\omega_t = \frac{1}{\sqrt{1+4\beta}}, \tag{5.11}$$

at which the wave vector reaches π and forms a standing wave. For $\omega \in [0, \omega_t]$ with the condition of $\beta > 0$, the group velocity dispersion $\partial^2 k/\partial\omega^2$ of the dispersion relation (5.10) can be shown to be always positive. In other words, the wave vector increases much more rapidly at higher frequencies. This justifies our claim that it is possible to significantly ruin the phase mismatch of processes involving higher frequency idlers through cutoff-frequency engineering and at the same time minimally affect the desired process that is at a much lower frequency. These two requirements have conflicting objectives and therefore altogether set up a upper and lower bound for the appropriate cut-off frequency. Figure 5-3 illustrates how fast the phase mismatch of three major sideband processes scales compared to that of the principle parametric amplification process Δk_1 as cut-off frequency ω_c decreases at a typical signal frequency $\omega_s = 5$GHz. The value of the phase mismatch ratio $|\Delta k_m/\Delta k_1|$ signifies how much larger in absolute magnitude the phase mismatch of the selected sideband processes are than the main amplification process, whereas the slope of the ratio $|\Delta k_m/\Delta k_1|$ represents how fast these phase mismatch terms grow compared to that of the principle process. We see that the slope of all three processes are non-negative as ω_c decreases initially, which means that we can indeed merit from

decreasing the cut-off frequency, although we do start see a diminishing return near very low ($\sim$ 40GHz) cut-off frequencies.

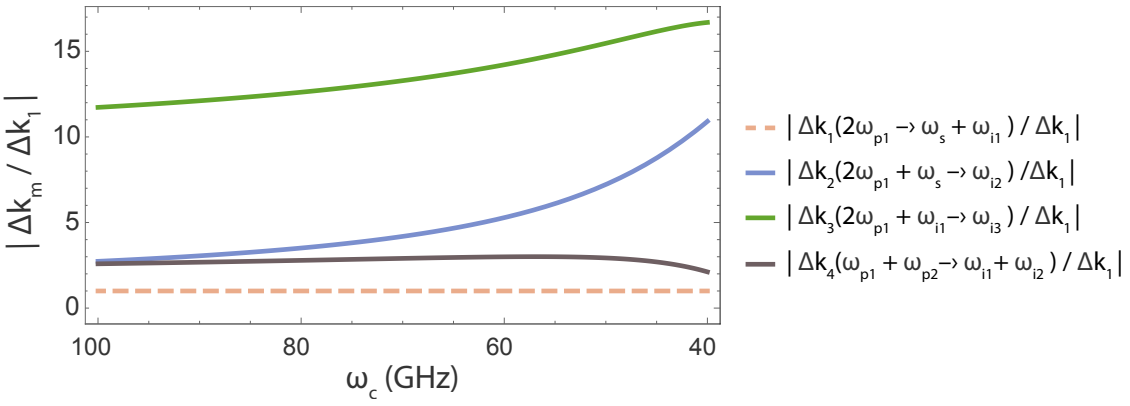

Figure 5-3: Phase mismatch ratios $|\Delta k_m/\Delta k_1|$ of prominent sideband processes as a function of decreasing cut-off frequency. Δk_1 (dashed) is the total phase mismatch of the principle parametric process. The remaining sideband processes (solid) are described in the legend.

Additionally, we would also like to address the issue of of the THG process of the pump, as we already saw in chapter 4 that the third harmonics of the pump can assist sideband interactions and negatively affect the quantum efficiency. We propose to create a stop band centered at the third harmonics of the pump by periodically modulate the impedance of the unit cells, similar to what was done in [28] and [50]. It is worth noting that in both of these works the principal photonic bandgap was opened up at the vicinity of the pump frequency, because their main objective is to utilize the dispersion at the band edge to achieve phase matching. In [28] an additional photonic bandgap was engineered near the third harmonics of the pump to increase the dynamic range and avoid a shock wave front [34], because the the high kinetic-inductance TiN coplanar waveguide is extremely linear (i.e. a very high cut-off frequency). In our case, we don't use the photonic bandgap for phase matching but for suppressing the third harmonics of the pump. Therefore, because we only place a photonic bandgap centered at the third harmonics of the pump, the dispersion at the

signal frequency range far away from the gap is minimally impacted. An additional benefit of having a photonic bandgap there is that it also helps further suppress the most problematic frequency conversion process $\gamma_{\omega_s} + 2\gamma_{\omega_{p1}} \rightarrow \gamma\omega_{i2}$, if the sideband ω_{i2} is also within or near the edge of the bandgap. This motivates us to make the gap width large by increasing the modulation depth. However, a larger modulation depth would result in would at the same decrease the maximum pump current, as the pump current has to be smaller than the minimum junction critical current in the modulated unit cells. Figure 5-4 plots the engineered dispersion of the proposed JTWPA design. The dispersion feature near 7 GHz is similarly introduced by period weakly coupled ground resonators, and a wide, $\sim$ 2.74 GHz bandgap centered at 21.71 GHz is created by a 15% modulation with a period of 6 unit cells. The cut-off frequency of this transmission line is chosen at $\sim$ 46 GHz to both suppress sideband process and properly place the photonic bandgap. The circuit parameters used to generate figure 5-4 is listed in table 5.1.

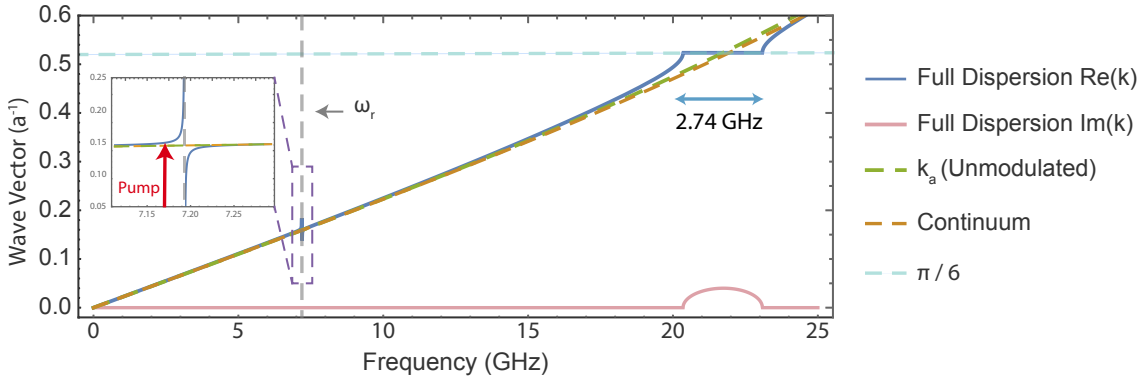

Figure 5-4: Engineered dispersion of the proposed high quantum efficiency JTWPA design. The real and imaginary component of the full engineered dispersion is plotted in solid blue and pink. The engineered dispersion has a weak resonance feature at $\omega_r/(2\pi) = 7.17$ GHz for phase matching. A $\sim$ 2.74 GHz photonic bandgap is opened at the third harmonics of the pump. The dispersion of an unmodulated transmission line described by (5.10) is plotted in dashed green, and the dispersion of a transmission line in the continuum limit is plotted in dashed orange. Inset is a close up of the dispersion at the phase matching resonance feature. The pump frequency is 7.17 GHz and is labeled by the red arrow in the inset.

I_0	C_0	C_J	PMR Period	Cut off Frequency (ω_c)
2.10 μA	51.9 fF	76.8 fF	3	45.6 GHz
C_r	L_r	C_c	Modulation Depth (δ)	Modulation Period
5.42 pF	0.09 pH	20 fF	15%	6 cells

Table 5.1: Circuit parameters for the proposed high quantum efficiency JTWPA design.

5.3.2 Predicted Gain Performance and Quantum Efficiency

table 5.1 summarizes one set of practical circuit parameters for the new JTWPA design that figure 5-5 corresponds to. In here, Panel (a) and (b) shows much cleaner gain dynamics as the lowest frequency sidebands ω_{i2} and ω_{i4} are strongly suppressed ($> 10dB$ differential). Panel (c) shows the gain, noise figure, and quantum efficiency spectrum of the new design, We see that for both pump conditions the quantum efficiency values are close to unity within a broad frequency range (5.8 to 8.8 GHz). The two spurious features near 5.8 GHz and 8.8 GHz are caused by one of the sidebands getting trapped/escaped from the photonic bandgap near the third harmonics of the pump.

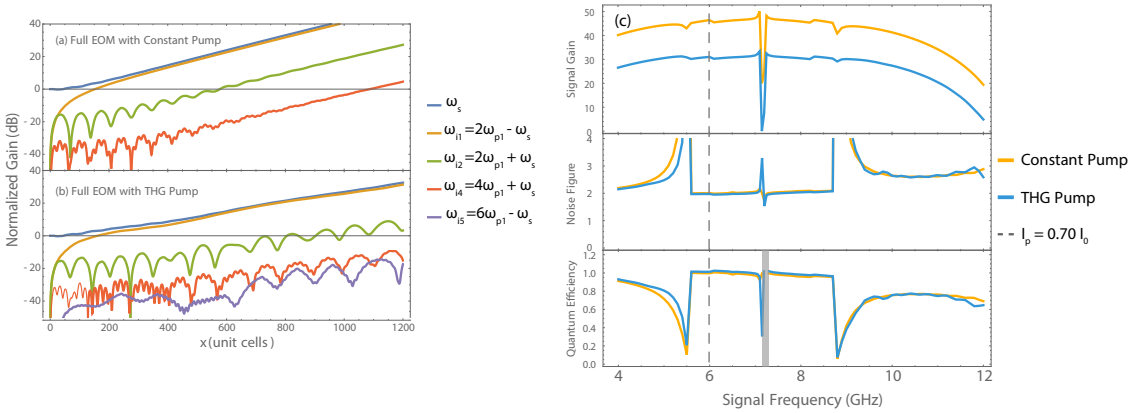

Figure 5-5: Gain dynamics of the proposed new JTWPA design as a function of position x using a (a) constant pump and (b) evanecent third harmonics of the pump. (c) plots the signal gain, noise figure, and quantum efficiency as a function of signal frequency. The pump frequency is 7.169GHz and the initial pump current is $I_p = 0.7IO_0$. SVEA was not used in the calculation.

5.3.3 Dynamic Range and Bandwidth Scaling

By forming a wide photonic bandgap centered around the third harmonics of the pump, we are able to significantly suppress the third harmonics of the pump and the adjacent idlers $\omega_{i2} = 2\omega_{p1} + \omega_s$ and $\omega_{i3} = 4\omega_{p1} - \omega_s$. Following the same argument as in Section 4.3 and [28], the absence of a non-trivial pump third harmonics increases the maximum allowed initial pump current to be used. Moreover, the suppression of the idlers ω_{i2} and ω_{i2} minimizes energy from being diverted from the principal signal and idler, thereby requiring less pump energy to achieve the same level of gain. These observations altogether project the dynamic range of our new JTWPA design to be at least on the same order as the existing ones.

Because the photonic bandgap is centered on the third harmonics and has minimal impact on dispersion at frequencies reasonably far apart, its effect on the signal gain bandwidth should be insignificant. However, the periodic modulation of the junctions decrease the smallest critical current, thereby reducing the dynamic range. However, the use of a lower cut-off frequency in linear design does concurrently increase the group velocity dispersion in the signal frequency range. In other words, the phase mismatch diverges away from the optimal frequency faster than it does on a "more linear" transmission line with a higher cutoff-frequency. We can estimate how the gain bandwidth scales with a reduced cutoff-frequency. The analytical expression (5.10) provides an excellent approximation to the full dispersion at the frequency range of interest. For a given pump condition, denote ω_{s0} to be the frequency at which the main parametric amplification process is perfectly matched with $\Delta k_0 \approx 0$. Assuming the changes in the total nonlinear phase mismatch from frequency detuning is minimal, we can taylor expand the phase mismatch Δk of a detuned signal frequency $\omega_s = \omega_s 0 + \epsilon$ around the optimal point to get

$$\begin{aligned}
\Delta_k(\epsilon) &\approx \Delta k_0 + \frac{\partial k}{\partial \omega}|_{\omega_0}(\omega_s - \omega_{s0}) + \frac{1}{2}\frac{\partial^2 k}{\partial \omega^2}|_{\omega_0}(\omega_s - \omega_{s0})^2 \\
&\approx \Delta k_0 - \frac{1}{4}\omega_0(1 + 12\beta)\epsilon^2 \\
&\approx -\frac{1}{4}\omega_0(1 + 12\beta)\epsilon^2. \qquad (5.12)
\end{aligned}$$

Notice that the (5.12) is written in the normalized unit, and we are only interested in the fixed frequency range in absolute units. To see the overall dependence on the cut-off frequency ω_c, we restore (5.12) into the absolute unit as

$$\begin{aligned}
\Delta_k(\epsilon) &\approx -\frac{1}{4}\tilde{\omega}_0(1+12\beta)\tilde{\epsilon}^2 \\
&= -\frac{1}{4}\frac{\omega_0}{\omega_c}\left(1+3\frac{\omega_c^2}{\omega_p^2}\right)\left(\frac{\epsilon}{\omega_c}\right)^2 \\
&\approx -\frac{1}{4}\frac{\omega_0}{\omega_c}\left(3\frac{\omega_c^2}{\omega_p^2}\right)\left(\frac{\epsilon}{\omega_c}\right)^2 \\
&= \left(-\frac{3}{4}\omega_0\right)\frac{\epsilon^2}{\omega_c}. \qquad (5.13)
\end{aligned}$$

We explicitly write the tildes on the first line of (5.13) to differentiate the normalized units to the absolute units in the final result. We dropped 1 from the $(1+12\beta)$ term because $12\beta \leq 9 > 1$ in the parameter of interest. Finally, we use equation (5.13) to evaluate the two pertinent criteria

$$\Delta k_{max} L = \pi \quad \Rightarrow \quad \epsilon_{max} \propto \sqrt{\omega_c} \quad \text{and} \qquad (5.14)$$

$$\Delta k_{max} \sim \kappa_s \propto \frac{\tilde{k}^4}{\tilde{\omega}^2} \quad \Rightarrow \quad \epsilon_{max} \propto 1/\sqrt{\omega_c}. \qquad (5.15)$$

equation (5.14) and (5.15) highlight the explicit dependence of signal gain bandwidth to the cut-off frequency ω_c. The first condition illustrates the how the coherence length scales with the cut-off frequency, and the second condition focuses on the relative magnitude of the coupling strength to the phase mismatch. It is clear that as we decrease the cutoff-frequency, the condition on coherence length is the dominant constraint which scales the signal gain bandwidth with the square root of the cut-off frequency. As a result, there is a trade-off between the quantum efficiency and the signal gain bandwidth through the adjustment of the cut-off frequency. Fortunately, the sideband population is much affected by the cut-off frequency in an exponential fashion(through phase mismatch). The 3dB bandwidth of our new design is approximately $\sqrt{\omega_{c,\text{new}}/\omega_{c,\text{old}}} \approx 0.72$ that of the existing design, which is still well in excess

of the typical bandwidth needed for current quantum experiments. In addition, with the suppression of higher order sidebands, our new design is predicted to achieve a higher peak gain. This means the the total gain bandwidth using the criterion of $> 20dB$ gain should be compensated correspondingly with an increased overall gain.

Chapter 6

Conclusion and Outlook

In this thesis, we developed a multi-mode model for the dynamics in JTWPAs which illustrates how higher order modes reduce the quantum efficiency. We proposed a new JTWPA design with both a reduced cut-off frequency and a photonic bandgap at the pump third harmonics to suppress sideband couplings and the pump THG process which improved the quantum efficiency. In future experimental work, we will fabricate and test such a device. In future theory work, we will investigate the assumption that the introduction of the photonic bandgap will effectively screen out the sidebands that fall into it. This is not entirely obvious in the nonlinear dynamics. We modeled the system dynamics in the continuum limit and treating each modulated unit cell to effectively have the same dispersion. However, the local structure of each unit cell does not prevent the generation of a wave inside the bandgap of the effective medium and it is unclear whether it will form a localized standing wave in the transmission line where a defect presents. In conclusion, we have studied the quantum efficiency of Josephson traveling wave parametric amplifiers, identified processes which reduce the quantum efficiency, and proposed new devices which have significantly higher quantum efficiency.

Bibliography

[1] Baleegh Abdo, Flavius Schackert, Michael Hatridge, Chad Rigetti, and Michel Devoret. Josephson amplifier for qubit readout. *Applied Physics Letters*, 99(16):162506, October 2011.

[2] Govind P Agrawal. Nonlinear fiber optics. In *Nonlinear Science at the Dawn of the 21st Century*, pages 195–211. Springer, 2000.

[3] Philip W Anderson and John M Rowell. Probable observation of the josephson superconducting tunneling effect. *Physical Review Letters*, 10(6):230, 1963.

[4] J. A. Armstrong, N. Bloembergen, J. Ducuing, and P. S. Pershan. Interactions between Light Waves in a Nonlinear Dielectric. *Physical Review*, 127(6):1918–1939, September 1962. Publisher: American Physical Society.

[5] John Bardeen, Leon N Cooper, and John Robert Schrieffer. Theory of superconductivity. *Physical review*, 108(5):1175, 1957.

[6] Alexandre Blais, Ren-Shou Huang, Andreas Wallraff, Steven M Girvin, and R Jun Schoelkopf. Cavity quantum electrodynamics for superconducting electrical circuits: An architecture for quantum computation. *Physical Review A*, 69(6):062320, 2004.

[7] R. Bonifacio, R. M. Caloi, and C. Maroli. The slowly varying envelope approximation revisited. *Optics Communications*, 101(3):185–187, August 1993.

[8] Vincent Bouchiat, D Vion, Ph Joyez, D Esteve, and MH Devoret. Quantum coherence with a single cooper pair. *Physica Scripta*, 1998(T76):165, 1998.

[9] Samuel Boutin, David M. Toyli, Aditya V. Venkatramani, Andrew W. Eddins, Irfan Siddiqi, and Alexandre Blais. Effect of Higher-Order Nonlinearities on Amplification and Squeezing in Josephson Parametric Amplifiers. *Physical Review Applied*, 8(5):054030, November 2017.

[10] Robert W Boyd. *Nonlinear optics*. Elsevier, 2003.

[11] M. A. Castellanos-Beltran, K. D. Irwin, L. R. Vale, G. C. Hilton, and K. W. Lehnert. Bandwidth and Dynamic Range of a Widely Tunable Josephson Parametric Amplifier. *IEEE Transactions on Applied Superconductivity*, 19(3):944–947, June 2009.

[12] Carlton M. Caves. Quantum limits on noise in linear amplifiers. *Physical Review D*, 26(8):1817–1839, October 1982.

[13] Carlton M Caves and David D Crouch. Quantum wideband traveling-wave analysis of a degenerate parametric amplifier. *JOSA B*, 4(10):1535–1545, 1987.

[14] A. A. Clerk, M. H. Devoret, S. M. Girvin, F. Marquardt, and R. J. Schoelkopf. Introduction to Quantum Noise, Measurement and Amplification. *Reviews of Modern Physics*, 82(2):1155–1208, April 2010. arXiv: 0810.4729.

[15] James I Colless, Vinay V Ramasesh, Dar Dahlen, Machiel S Blok, ME Kimchi-Schwartz, JR McClean, J Carter, WA De Jong, and I Siddiqi. Computation of molecular spectra on a quantum processor with an error-resilient algorithm. *Physical Review X*, 8(1):011021, 2018.

[16] Leon N Cooper. Bound electron pairs in a degenerate fermi gas. *Physical Review*, 104(4):1189, 1956.

[17] David Deutsch and Richard Jozsa. Rapid solution of problems by quantum computation. *Proceedings of the Royal Society of London. Series A: Mathematical and Physical Sciences*, 439(1907):553–558, 1992.

[18] Michel H Devoret, Andreas Wallraff, and John M Martinis. Superconducting qubits: A short review. *arXiv preprint cond-mat/0411174*, 2004.

[19] Tom Dixon, Jacob W Dunstan, George B Long, Jonathan M Williams, Phil J Meeson, and Connor D Shelly. Capturing complex behaviour in josephson travelling wave parametric amplifiers. *arXiv preprint arXiv:1912.05349*, 2019.

[20] Christopher Eichler and Andreas Wallraff. Controlling the dynamic range of a Josephson parametric amplifier. *EPJ Quantum Technology*, 1(1):2, January 2014.

[21] Tamer S EL-Sayed and S EL-Rabaie. Comparative study of time domain, harmonic balance and volterra series methods for nonlinear circuit simulation. *Menoufia Journal of Electronic Engineering Research*, 21(2):167–186, 2011.

[22] Arne L. Grimsmo and Alexandre Blais. Squeezing and quantum state engineering with Josephson travelling wave amplifiers. *npj Quantum Information*, 3(1):20, June 2017. tex.ids: grimsmo_squeezing_2017-1.

[23] Lov K Grover. A fast quantum mechanical algorithm for database search. In *Proceedings of the twenty-eighth annual ACM symposium on Theory of computing*, pages 212–219, 1996.

[24] Shay Hacohen-Gourgy, Leigh S Martin, Emmanuel Flurin, Vinay V Ramasesh, K Birgitta Whaley, and Irfan Siddiqi. Quantum dynamics of simultaneously measured non-commuting observables. *Nature*, 538(7626):491–494, 2016.

[25] H. A. Haus and J. A. Mullen. Quantum Noise in Linear Amplifiers. *Physical Review*, 128(5):2407–2413, December 1962.

[26] H. Heffner. The Fundamental Noise Limit of Linear Amplifiers. *Proceedings of the IRE*, 50(7):1604–1608, July 1962. Conference Name: Proceedings of the IRE.

[27] Johannes Heinsoo, Christian Kraglund Andersen, Ants Remm, Sebastian Krinner, Theodore Walter, Yves Salathé, Simone Gasparinetti, Jean-Claude Besse, Anton Potočnik, Christopher Eichler, and Andreas Wallraff. Rapid high-fidelity multiplexed readout of superconducting qubits. *Physical Review Applied*, 10(3):034040, September 2018. arXiv: 1801.07904.

[28] Byeong Ho Eom, Peter K. Day, Henry G. LeDuc, and Jonas Zmuidzinas. A wideband, low-noise superconducting amplifier with high dynamic range. *Nature Physics*, 8(8):623–627, August 2012.

[29] M. Houde, L. C. G. Govia, and A. A. Clerk. Loss asymmetries in quantum travelling wave parametric amplifiers. *arXiv:1809.07418 [cond-mat, physics:quant-ph]*, September 2018. arXiv: 1809.07418.

[30] BRIAN D Josephson. The discovery of tunnelling supercurrents. *Reviews of Modern Physics*, 46(2):251, 1974.

[31] H Kamerlingh Onnes. The resistance of pure mercury at helium temperatures. *Commun. Phys. Lab. Univ. Leiden, b*, 120, 1911.

[32] Bruce E Kane. A silicon-based nuclear spin quantum computer. *nature*, 393(6681):133–137, 1998.

[33] Jens Koch, M Yu Terri, Jay Gambetta, Andrew A Houck, DI Schuster, J Majer, Alexandre Blais, Michel H Devoret, Steven M Girvin, and Robert J Schoelkopf. Charge-insensitive qubit design derived from the cooper pair box. *Physical Review A*, 76(4):042319, 2007.

[34] Rolf Landauer. Shock waves in nonlinear transmission lines and their effect on parametric amplification. *IBM Journal of Research and Development*, 4(4):391–401, 1960.

[35] Nathan K Langford. Circuit qed-lecture notes. *arXiv preprint arXiv:1310.1897*, 2013.

[36] Hervé Leblond and Dumitru Mihalache. Few-optical-cycle solitons: Modified korteweg–de vries sine-gordon equation versus other non–slowly-varying-envelope-approximation models. *Physical Review A*, 79(6):063835, 2009.

[37] Anthony J Leggett. Macroscopic quantum systems and the quantum theory of measurement. *Progress of Theoretical Physics Supplement*, 69:80–100, 1980.

[38] C. Macklin, K. O'Brien, D. Hover, M. E. Schwartz, V. Bolkhovsky, X. Zhang, W. D. Oliver, and I. Siddiqi. A near–quantum-limited Josephson traveling-wave parametric amplifier. *Science*, 350(6258):307–310, October 2015.

[39] Christopher Stewart Macklin. *Quantum Feedback and Traveling-wave Parametric Amplification in Superconducting Circuits*. PhD thesis, UC Berkeley, 2015.

[40] Esteban A Martinez, Christine A Muschik, Philipp Schindler, Daniel Nigg, Alexander Erhard, Markus Heyl, Philipp Hauke, Marcello Dalmonte, Thomas Monz, Peter Zoller, et al. Real-time dynamics of lattice gauge theories with a few-qubit quantum computer. *Nature*, 534(7608):516–519, 2016.

[41] Nicholas A. Masluk, Ioan M. Pop, Archana Kamal, Zlatko K. Minev, and Michel H. Devoret. Microwave Characterization of Josephson Junction Arrays: Implementing a Low Loss Superinductance. *Physical Review Letters*, 109(13):137002, September 2012.

[42] C. J. McKinstrie, S. Radic, and M. G. Raymer. Quantum noise properties of parametric amplifiers driven by two pump waves. *Optics Express*, 12(21):5037–5066, October 2004.

[43] Xiao Mi, JV Cady, DM Zajac, PW Deelman, and Jason R Petta. Strong coupling of a single electron in silicon to a microwave photon. *Science*, 355(6321):156–158, 2017.

[44] Chris Monroe, DM Meekhof, BE King, Wayne M Itano, and David J Wineland. Demonstration of a fundamental quantum logic gate. *Physical review letters*, 75(25):4714, 1995.

[45] Michael J. Morgan. Lagrangian formulation of a transmission line. *American Journal of Physics*, 56(7):639–643, July 1988.

[46] Engineering National Academies of Sciences. *Quantum Computing: Progress and Prospects*. December 2018.

[47] Kevin O'Brien, Chris Macklin, Irfan Siddiqi, and Xiang Zhang. Resonantly phase-matched Josephson junction traveling wave parametric amplifier. *Physical Review Letters*, 113(15), October 2014. arXiv: 1406.2346.

[48] Kevin Patrick O'Brien. *Nonlinear Light-Matter Interactions in Metamaterials*. PhD thesis, UC Berkeley, 2016.

[49] Christophe Pierre, AA Ferri, and EH Dowell. Multi-harmonic analysis of dry friction damped systems using an incremental harmonic balance method. 1985.

[50] Luca Planat, Arpit Ranadive, Rémy Dassonneville, Javier Puertas Martínez, Sébastien Léger, Cécile Naud, Olivier Buisson, Wiebke Hasch-Guichard, Denis M. Basko, and Nicolas Roch. Photonic-Crystal Josephson Traveling-Wave Parametric Amplifier. *Physical Review X*, 10(2):021021, April 2020. Publisher: American Physical Society.

[51] David M Pozar. *Microwave Engineering 3e*. Wiley, 2006.

[52] Steven Prawer and Andrew D Greentree. Diamond for quantum computing. *Science*, 320(5883):1601–1602, 2008.

[53] H. Puell and C. Vidal. Optimum conditions for nonresonant third harmonic generation. *IEEE Journal of Quantum Electronics*, 14(5):364–373, May 1978. Conference Name: IEEE Journal of Quantum Electronics.

[54] Jinendra K Ranka and Alexander L Gaeta. Breakdown of the slowly varying envelope approximation in the self-focusing of ultrashort pulses. *Optics Letters*, 23(7):534–536, 1998.

[55] Joshua E Rothenberg. Space–time focusing: breakdown of the slowly varying envelope approximation in the self-focusing of femtosecond pulses. *Optics Letters*, 17(19):1340–1342, 1992.

[56] Tanay Roy, Suman Kundu, Madhavi Chand, A. M. Vadiraj, A. Ranadive, N. Nehra, Meghan P. Patankar, J. Aumentado, A. A. Clerk, and R. Vijay. Broadband parametric amplification with impedance engineering: Beyond the gain-bandwidth product. October 2015.

[57] David J. Santos and Rodney Loudon. Electromagnetic-field quantization in inhomogeneous and dispersive one-dimensional systems. *Physical Review A*, 52(2):1538–1549, August 1995. Publisher: American Physical Society.

[58] D. I. Schuster, A. Wallraff, A. Blais, L. Frunzio, R.-S. Huang, J. Majer, S. M. Girvin, and R. J. Schoelkopf. ac Stark Shift and Dephasing of a Superconducting Qubit Strongly Coupled to a Cavity Field. *Physical Review Letters*, 94(12):123602, March 2005. tex.ids: schuster_ac_2005-1, schuster_ac_2005-2.

[59] Peter W Shor. Polynomial-time algorithms for prime factorization and discrete logarithms on a quantum computer. *SIAM review*, 41(2):303–332, 1999.

[60] Michael Tinkham. *Introduction to superconductivity*. Courier Corporation, 2004.

[61] Sergey K Tolpygo, Vladimir Bolkhovsky, Terence J Weir, Leonard M Johnson, Mark A Gouker, and William D Oliver. Fabrication process and properties of fully-planarized deep-submicron nb/al-alox/nb josephson junctions for vlsi circuits. *IEEE transactions on Applied Superconductivity*, 25(3):1–12, 2014.

[62] Olof Tornblad, Choshu Ito, Francis Rotella, Gordon Ma, and Robert W Dutton. Linearity analysis of rf ldmos devices utilizing harmonic balance device simulation. In *2005 International Conference On Simulation of Semiconductor Processes and Devices*, pages 243–246. IEEE, 2005.

[63] Thomas Torounidis, Peter A Andrekson, and B-E Olsson. Fiber-optical parametric amplifier with 70-db gain. *IEEE Photonics Technology Letters*, 18(10):1194–1196, 2006.

[64] D.M. Toyli, A.W. Eddins, S. Boutin, S. Puri, D. Hover, V. Bolkhovsky, W.D. Oliver, A. Blais, and I. Siddiqi. Resonance Fluorescence from an Artificial Atom in Squeezed Vacuum. *Physical Review X*, 6(3):031004, July 2016.

[65] R. Vijay, M. H. Devoret, and I. Siddiqi. Invited Review Article: The Josephson bifurcation amplifier. *Review of Scientific Instruments*, 80(11):111101, November 2009.

[66] T. C. White, J. Y. Mutus, I.-C. Hoi, R. Barends, B. Campbell, Yu Chen, Z. Chen, B. Chiaro, A. Dunsworth, E. Jeffrey, J. Kelly, A. Megrant, C. Neill, P. J. J. O'Malley, P. Roushan, D. Sank, A. Vainsencher, J. Wenner, S. Chaudhuri, J. Gao, and John M. Martinis. Traveling wave parametric amplifier with Josephson junctions using minimal resonator phase matching. *Applied Physics Letters*, 106(24):242601, June 2015.

[67] O. Yaakobi, L. Friedland, C. Macklin, and I. Siddiqi. Parametric amplification in josephson junction embedded transmission lines. *Physical Review B*, 87(14):144301, April 2013.

[68] Oded Yaakobi, Lazar Friedland, Chris Macklin, and Irfan Siddiqi. Erratum: Parametric amplification in josephson junction embedded transmission lines [phys. rev. b 87, 144301 (2013)]. *Physical Review B*, 88(21):219904, December 2013.

[69] B Yurke, LR Corruccini, PG Kaminsky, LW Rupp, AD Smith, AH Silver, RW Simon, and EA Whittaker. Observation of parametric amplification and deamplification in a josephson parametric amplifier. *Physical Review A*, 39(5):2519, 1989.

[70] Ting Zhou, Danzhi Huang, and Amedeo Caflisch. Quantum mechanical methods for drug design. *Current topics in medicinal chemistry*, 10(1):33–45, 2010.

[71] A.B. Zorin. Flux-Driven Josephson Traveling-Wave Parametric Amplifier. *Physical Review Applied*, 12(4):044051, October 2019. Publisher: American Physical Society.